Zhang Xiaoxin (Orcid ID: 0000-0002-7759-7402)
He Fei (Orcid ID: 0000-0003-0542-2686)
Fok Mei-Ching, H. (Orcid ID: 0000-0001-9500-866X)
Liemohn Michael, W. (Orcid ID: 0000-0002-7039-2631)
Gallagher Dennis (Orcid ID: 0000-0003-3924-3571)

A new solar wind driven global dynamic plasmapause model: 1. Database and Statistics

Xiao-Xin Zhang, Key Laboratory of Space Weather, National Center for Space Weather, China Meteorological Administration, Beijing, China (Email: xxzhang@cma.gov.cn)

Fei He, Key Laboratory of Earth and Planetary Physics, Institute of Geology and Geophysics, Chinese Academy of Sciences, Beijing, China (**Corresponding author, Email: hefei@mail.iggcas.ac.cn**)

Rui-Lin Lin, National Space Science Center, Chinese Academy of Sciences, Beijing, China (Email: linrl@nssc.ac.cn)

Mei-Ching Fok, NASA Goddard Space Flight Center, Code 673, Greenbelt, MD 20771, USA (Email: mei-ching.h.fok@nasa.gov)

Roxanne M. Katus, Department of Mathematics, Eastern Michigan University, Ypsilanti, Michigan, USA (Email: rkatus@emich.edu)

Michael W. Liemohn, Department of Climate and Space Sciences and Engineering, Ann Arbor, Michigan, USA (Email: liemohn@umich.edu)

Dennis L. Gallagher, NASA Marshall Space Flight Center, Huntsville, Alabama, USA (Email: dennis.gallagher@nasa.gov)

Shinya Nakano, The Institute of Statistical Mathematics, Tachikawa, Tokyo, Japan (Email:

This is the author manuscript accepted for publication and has undergone full peer review but has not been through the copyediting, typesetting, pagination and proofreading process, which may lead to differences between this version and the Version of Record. Please cite this article as doi: 10.1002/2017JA023912

shiny@ism.ac.jp)

Abstract.

A large database, possibly the largest plasmapause location database, with 49119 plasmapause crossing events from the in-situ observations and 3957 plasmapause profiles (corresponding to 48899 plasmapause locations in 1 h MLT intervals) from optical remote sensing from 1977 to 2015 by 18 satellites is compiled. The responses of the global plasmapause to solar wind and geomagnetic changes and the diurnal, seasonal, solar cycle variations of the plasmapause are investigated based on this database. It is found that the plasmapause shrinks towards the Earth globally and a clear bulge appears in the afternoon to pre-midnight MLT sector as the solar wind or geomagnetic conditions change from quiet to disturbed. The bulge is clearer during storm times or southward IMF. The diurnal variations of the plasmapause are most probably be result of the difference between the magnetic dipole tilt and the Earth's spin axis. The seasonal variations of the plasmapause are characterized by equinox valleys and solstice peaks. It is also found that the plasmapause approaches the Earth during high solar activity and expands outward during low solar activity. This database will help us study and understand the evolution properties of the plasmapause shape and the interaction processes of the plasmasphere, the ring current and the radiation belts in the magnetosphere.

Key Points:

1. The largest currently available plasmapause location database is compiled based on observations from 18 satellites from 1977 to 2015
2. This database reveals the responses of the global plasmapause locations to solar wind and

geomagnetic changes

3. The plasmapause locations exhibit clear MLT-dependent diurnal, seasonal, and solar cycle variations

1. Introduction

The plasmasphere is a torus of cold (~1 eV) and dense (electron density of the order of 100 – 10,000 cm^{-3}) plasma region surrounding the Earth with the ionospheric originated electrons and ions all trapped on geomagnetic field lines [*Lemaire and Gringauz*, 1998; *Sandel et al.*, 2003; *Kotova*, 2007; *Darrouzet et al.*, 2009]. The plasmapause, the outer boundary of the plasmasphere, is often defined as a transition region in which the plasma density usually exhibits a drop of at least half an order of magnitude in less than one Earth radius (R_E, 1 R_E=6378.0 km) of altitude [*Carpenter*, 1963, 1966; *Gringauz*, 1963; *Carpenter and Anderson*, 1992]. Since the cold plasma in the plasmasphere is primarily subject to **E** × **B** drift, the plasmapause position is essential in the determination of the inner magnetospheric convections, and it is usually located at geocentric distances of 3.0 – 6.0 R_E on the geomagnetic equatorial plane [*Lemaire and Gringauz*, 1998]. The location of the plasmapause reveals the important interactions of the plasmasphere with the magnetospheric convection and responds to changes in the strength of geomagnetic activity in the inner magnetosphere [e.g., *Goldstein et al.*, 2003a]. It is inferred from several reviews [e.g., *Ganguli et al.*, 2000; *Liemohn*, 2006; *Kotova*, 2007; *Darrouzet et al.*, 2009; *Pierrard et al.*, 2009] that the dynamic location of the plasmapause may contribute to the particle precipitation and/or loss (due to wave-particle interaction) of the ring current and the radiation belts, since the plasmasphere, the ring current and the radiation belts are overlapped in the magnetosphere [*Carpenter and Anderson*, 1992; *Carpenter*, 1995; *Fok et al.*, 1995; *Khazanov and Liemohn*, 1995; *Goldstein et al.*, 2003a; *Spasojević et al.*, 2003].

In the past four decades, many types of instruments have been launched into space to characterize the plasmaspheric density structures and dynamics through in-situ measurements and remote sensing [*Carpenter*, 2004; *Goldstein*, 2006; *Gallagher and Comfort*, 2016]. Typical instruments are summarized as follows.

1. Mass spectrometer. Measurements of the positive ion concentration by ion traps on Russian satellites in 1950–1959 were the first to discover the plasmasphere and its outer boundary at 4 R_E [*Gringauz*, 1963; *Lemaire and Gringauz*, 1998, and references therein]. *Chappell et al.* [1970] and *Harris et al.* [1970] studied the influence of magnetic activity on the plasmapause locations using the measurements from the light ion mass spectrometer aboard OGO 5 [*Harris and Sharp*, 1969]. Other examples include the retarding ion mass spectrometer on Dynamics Explorer 1 (DE 1), which also provided many in-situ measurements of plasmaspheric ion composition and structure [e.g., *Comfort et al.*, 1985; *Olsen et al.*, 1987; *Newberry et al.*, 1989], and the low-energy plasma instruments on the Van Allen Probes, that have provided useful data for plasmaspheric studies [e.g., *Sarno-Smith et al.*, 2016].
2. Plasma wave instruments. The electron density profiles deduced from the sweep frequency receiver (SFR) measurements on the International Sun-Earth Explorer (ISEE-1) [*Ogilvie et al.*, 1977] were used to develop the first empirical model of the equatorial electron density in the magnetosphere [*Carpenter and Anderson*, 1992]. From the 1980's on, many plasma wave instruments were used to measure the electron density of the plasmasphere, such as those aboard DE 1 [*Shawhan et al.*, 1981], the Exosphere D satellite (EXOS-D, also known as Akebono)

[*Tsuruda and Oya*, 1991], the Combined Release and Radiation Effects Satellite (CRRES) [*Anderson et al.*, 1992], the Polar satellite [*Gurnett et al.*, 1995], the Imager for Magnetosphere-to-Auroral Global Exploration (IMAGE) [*Burch*, 2000], the Cluster [*Décréau et al.*, 1997], and the Van Allen Probes (VAP) [*Kletzing et al.*, 2013]. Measurements by these plasma wave experiments have greatly advanced our understanding on the dynamics of the plasmasphere (and the plasmapause).

3. Optical remote sensing. The extreme ultraviolet imager (EUV) aboard the IMAGE mission [*Sandel et al.*, 2000] provided for the first time the global EUV images of plasmaspheric He^+ from polar perspectives for studying the global structures of the plasmasphere. The telescope of extreme ultraviolet (TEX) aboard the Selenological and Engineering Explorer (SELENE) (also known as KAGUYA) [*Yoshikawa et al.*, 2008] launched in 2008 and the EUV Camera (EUVC) aboard the Chang'e-3 mission [*Chen et al.*, 2014] launched in 2013 provided the global EUV images of plasmasphere He^+ from the side perspective. In the plasmaspheric EUV images, the plasmapause was identified as the outermost sharp edge where the intensity of the 30.4 nm emissions drops abruptly [*Goldstein et al.*, 2003a; *He et al.*, 2016].
4. Electro-static analyzer. The Time History of Events and Macroscale Interactions during Substorms (THEMIS) launched in 2007 provided the total electron density from spacecraft potential and electron thermal velocity [*Angelopoulos*, 2008], from which several plasmapause models were constructed [*Cho et al.*, 2015; *Liu et al.*, 2015; *Verbanac et al.*, 2015]. This has also been done with the magnetospheric plasma analyzer (MPA) instrument on the geosynchronously

orbiting spacecraft operated by the Los Alamos National Laboratory [e.g., *Moldwin et al.*, 1995; *Lawrence et al.*, 1999].

Numerous studies have demonstrated that the shape and geocentric distance of the plasmapause are highly dependent on the geomagnetic and solar wind conditions [e.g., *Chappell et al.*, 1970; *Grebowsky*, 1970; *Horwitz et al.*, 1990; *Carpenter and Anderson*, 1992; *Moldwin et al.*, 2002; *O'Brien and Moldwin*, 2003; *Goldstein et al.*, 2003b, 2005; *Gallagher et al.*, 2005; *Larsen et al.*, 2007; *Cho et al.*, 2015; *Liu et al.*, 2015; *Verbanac et al.*, 2015; *Katus et al.*, 2015; *Bandić et al.*, 2016]. Based on the correlations of the plasmapause with geomagnetic indices such as *Kp*, *Dst*, and *AE* and solar wind parameters such as the *z* component of the interplanetary magnetic field (IMF B_Z), the solar wind speed, and some energy coupling functions, several empirical or statistical models of the plasmapause locations have been developed. For example, *Carpenter and Anderson* [1992] derived the well know *Kp*-dependent plasmapause location model using ISEE-1 data. *Moldwin et al.* [2002] and *O'Brien and Moldwin* [2003] built empirical models of the plasmapause locations as functions of the most recent maximum in *AE* or minimum in *Dst* based on a database of CRRES observations. *Larsen et al.* [2007] obtained the plasmapause location model as a function of IMF B_Z, IMF clock angle (θ) and a merging proxy (the Kan-Lee electric field, $\boldsymbol{\phi}=vB^2\sin^2(\theta/2)$) using the IMAGE EUV images. *Cho et al.* [2015] constructed a plasmapause model as a function of IMF B_Z, solar wind flow speed, and *AE* based on THEMIS observations, and *Liu et al.* [2015] used the same observation data to establish an MLT-dependent dynamic plasmapause location model characterized by the *SYM-H*, *AL*, *AU*, *AE*, and *Kp* indices. It is noted that the above mentioned plasmapause location models were built based on limited periods of data. The MLT-dependence was not included in some of these models because of the limited coverage of the database. The MLT-dependent diurnal, seasonal, and solar cycle variations of the plasmapause have not been fully addressed in these models.

In this paper, a large plasmapause locations database covering the observations from 1977 to 2015 has been compiled to study the global variations of plasmapause locations in different time scales with different geomagnetic indices and solar wind and IMF parameters. A new solar wind driven global dynamic plasmapause model will be developed based on statistical investigations of the database and will be presented in the companion paper [*He et al.*, this issue]. The outline of the paper is as follows. The observation data, plasmapause extraction methods, and the establishment of the large plasmapause database are introduced in detail in section 2. The statistical analysis of the global shape variations and the MLT-dependent diurnal, seasonal and solar cycle variations of the plasmapause will be presented in section 3. A summary and conclusion will be given in section 4.

2. Data and Methodology

2.1. Overview of Data

In this investigation, there are two kinds of plasmapause location data obtained from different instruments aboard different satellites listed in Table 1. Among these data, 49119 plasmapause crossings have been extracted from the in-situ plasma wave instruments, e.g., the Plasma Wave Investigation (PWI) on ISEE-1 [*Ogilvie et al.*, 1977; *Gurnett et al.*, 1978], the Plasma Wave and Quasi-Static Electric Field Instrument (PWI) on DE-1 [*Shawhan et al.*, 1981; *Gurnett and Inan*, 1988], the Plasma Wave Observation and Sounder Experiments (PWS) on Akebono [*Tsuruda and Oya*, 1991; *Oya et al.*, 1990], the Plasma Wave Experiment (PWE) on CRRES [*Anderson et al.*, 1992], the Plasma Wave Instrument (PWI) and Electric Field Instrument (EFI) on Polar [*Gurnett et al.*, 1995; *Harvey et al.*, 1995], the Radio Plasma Imager (RPI) [*Reinisch et al.*, 2000] on IMAGE [*Burch*, 2000], the Waves of High frequency and Sounder for Probing of Electron density by Relaxation (WHISPER) on Cluster [*Décréau et al.*, 1997; *Darrouzet et al.*, 2002], the Electric Field Instrument (EFI) and the Electro-Static Analyzer (ESA) on THEMIS [*McFadden et al.*, 2008; *Bonnell et al.*, 2008], and the Electric and Magnetic Field Instrument Suite and Integrated Science (EMFISIS) on VAP [*Kletzing et al.*, 2013; *Kurth et al.*, 2015].

Based on the plasmaspheric images observed by the IMAGE EUV imager [*Sandel et al.*, 2000] and the CE-3 EUVC instrument [*Chen et al.*, 2014; *He et al.*, 2016], the plasmapause locations on the magnetic equatorial plane were reconstructed with the Minimum L Algorithm (MLA, see Appendix). In total, 3579 and 378 plasmaspheric images were selected from IMAGE EUV from 2000 to 2002 and from CE-3 EUVC in 2014, respectively, and 48899 plasmapause locations were obtained in 1 h MLT intervals.

The data intervals, satellite names and instruments for these available plasmaspheric observations are listed in Table 1 and are also shown in Figure 1. The orbits of these satellites corresponding to Table 1 are plotted in Figure 2 (only the trajectories around the beginning, the first quarter, the middle, and the third quarter of an orbital regression cycle are plotted). The orbital regression cycle of CRRES and VAP is approximately two years and that of the other satellites except CE-3 is one year, making all of magnetic local time (MLT) sampled. It is noted that the CE-3 lunar lander is on the lunar surface (~60 R_E away from the Earth) and the plasmaspheric images from EUVC were only obtained in the magnetic local time (MLT) sector between 4.0 h and 6.0 h [*He et al.*, 2016].

All the data were obtained during the period from November 1977 to December 2015 (more than 38 years), covering almost four solar cycles (21, 22, 23, and 24). The plasmaspheric observations in this investigation include two types, one is the in-situ measurements (plasma wave instruments and electro-static analyzers) and the other is from optical remote sensing. The detailed plasmapause determination criteria for the plasmaspheric observations will be described in detail in the following sections.

2.2. Plasmapause Determination from In-situ Crossings

For the plasma wave instruments (ISEE-1 PWI, DE-1 PWI, Akebono PWS, CRRES PWE, Polar PWI, IMAGE RPI, Cluster WHISPER, and VAP EMFISIS), a typical signature in the frequency-time spectrograms is the upper hybrid resonance (UHR) frequency (f_{UHR}, in Hz). The electron density (n_e, in cm^{-3}) can be related to f_{UHR} through the following formula [*Kurth et al.*, 2015]:

$$n_e = \frac{f_{UHR}^2 - f_{ce}^2}{8980^2} \qquad (1)$$

where $f_{ce}=eB/m_e$ is the electron cyclotron frequency, B is the strength of the magnetic field in nT, e is the electron charge, and m_e is the electron mass. Here, f_{ce} is estimated with the IGRF internal magnetic field model combined with the Tsyganenko 2007 external magnetic field model

[*Tsyganenko and Sitnov*, 2007; *Sitnov et al.*, 2008] since not all the satellites are equipped with a scientific magnetometer. This method of deducing electron densities has been successfully applied to all the plasma wave instruments in many studies [*Oya et al.*, 1990; *Moldwin et al.*, 2002; *Goldstein et al.*, 2003a; *Darrouzet et al.*, 2004; *Kurth et al.*, 2015; and *references therein*] with an accuracy close to 10% [*Goldstein et al.*, 2014; *Kurth et al.*, 2015]. Examples of the frequency-time spectrograms of the in-situ plasma wave environment and the electron densities deduced from f_{UHR} are shown in Figure 3.

For the THEMIS satellites, the spacecraft potential (refers to the potential of the spacecraft body relative to the ambient plasma) measured by the EFI and the electron thermal velocities measured by the ESA are used to calculate the electron density with the detailed method described in *Mozer* [1973] and *Pedersen et al.* [1998]. The calculated electron densities are associated with an error of a factor of 2, which is smaller than the density drop around the plasmapause, and have been widely used to identify the plasmapause locations [*Li et al.*, 2010; *Cho et al.*, 2015; *Liu et al.*, 2015]. An example of the electron density profile and corresponding satellite potential is shown in Figure 4*a*-4*b*.

For the Polar satellite, the electron densities inferred from the spacecraft potential measured by EFI [*Scudder et al.*, 2000; *Kim et al.*, 2010] were used to determine the plasmapause locations after 16 September 1997 when the PWI data were unavailable. An example of the electron density profile and corresponding satellite potential is shown in Figure 4*c*-4*d*.

As widely adopted in previous studies [*Carpenter and Anderson*, 1992; *Moldwin et al.*, 2002;

Darrouzet et al., 2013; *Cho et al.*, 2015; *Kwon et al.*, 2015; *Liu et al.*, 2015], a density drop of a factor of 5 or more over an *L* distance smaller than 0.5 is required for a plasmapause crossing. This criterion is also adopted in this investigation. Finally, the plasmapause locations identified from the deduced electron density profiles are shown by the vertical red dashed lines in Figures 3 and 4.

2.3. Plasmapause Determination from Optical Imagers

For the EUV imaging instruments onboard IMAGE and CE-3, various techniques [*Roelof and Skinner*, 2000; *Sandel et al.*, 2003; *Wang et al.*, 2006, 2007; *He et al.*, 2011, 2012, 2016] have been developed to interpret the plasmapause locations. In this investigation, the MLA technique [*Wang et al.*, 2007; *He et al.*, 2011, 2016] is used to determine the plasmapause locations from the EUV images. In the EUV images, each pixel corresponds to a line of sight (LOS) integration of the resonantly scattered sunlight at 30.4 nm with the emission intensity proportional to the column integrated density of He^+ along the LOS. A typical signature in a plasmaspheric EUV image is the sharp edge where the brightness of 30.4 nm He^+ emissions drops abruptly. This sharp edge can reliably be treated as the plasmapause outline [*Goldstein et al.*, 2003a; *He et al.*, 2011, 2016]. For each pixel in the outline boundary, the corresponding LOS is calculated, and all the magnetic field lines intersected by the LOS are traced onto the magnetic equator to get the field line with minimum *L* value which is treated as the plasmapause. Different pixels in the outline boundary correspond to different MLTs when traced onto the magnetic equator and the MLT-dependence of the plasmapause location can be finally determined by the MLA. Detailed description of the MLA can be found in the Appendix and the supporting information. Examples of plasmapause profiles extracted from an

IMAGE EUV image obtained at 14:14 UT on 26 June 2000 and a CE-3 EUVC image taken at 13:01 UT on 21 April 2014 are shown in Figure 5. It is noted that only the plasmaspheric EUV images with sharp edges with radial intensity drops of at least one order of magnitude are analyzed to ensure the reliability of the results, the MLT sectors with multiple plasmapauses are also excluded, and the plasmapause locations determined from EUV or EUVC are resampled into 1.0 h MLT intervals.

2.4. Comparisons between Different Satellites

To verify the consistency between the plasmapause locations extracted from different satellites with different methods, comparisons between different satellites are conducted. Our purpose is to check whether the plasmapause locations observed by two different satellites at the same UT and same MLT have the same L-values. Due to the orbital differences between different satellites, it is almost impossible to find exact simultaneous plasmapause crossings. Therefore, a time window of 20 min and a MLT window of 1 h are adopted to search the plasmapause locations that are almost simultaneously observed by two satellites. For a plasmapause location observed by satellite A (A can be any satellite listed in Table 1) and parameterized by UT_A, MLT_A, and L_A (calculation of MLT and L is introduced in the next section), the plasmapause location parameterized by UT_B, MLT_B, and L_B observed satellite B (B can be any satellite listed in Table 1 with B ≠ A) is automatically searched out if $|UT_A – UT_B| < 20$ min and $|MLT_A – MLT_B| < 1$ h. For each satellite pair (e.g., A-B), a sub-database of L_A and L_B pairs is established. After all the satellite pairs are processed using the above procedure, 8 sub-databases with a total of 1045 L_A-L_B pairs are established as shown in

Figure 6. The number of L_A-L_B pairs in each sub-database is shown at the lower right corner of each panel in Figure 6.

If the plasmapause locations determined from two different satellites agree perfectly, all the circles would lie along the red solid lines ($L_A = L_B$) in Figure 6. Actually, 95% of the circles are within 0.5 R_E of perfect agreement. The dashed lines in each panel are drawn at $L_A = L_B \pm 0.5\ R_E$ for reference. The linear correlations between L_A and L_B are all larger than 0.8 (highly significant) as shown by the red numbers in each panel in Figure 6. This indicates that the plasmapause locations determined from different types of plasmaspheric observations are consistent and our plasmapause determination methods are reasonable and reliable for further statistical investigation and model establishment. Therefore, the resulting error estimated for determining the plasmapause location for each data source is less than 0.5 R_E.

2.5. Plasmapause Location Database Compilation

Using the above-introduced methods and criteria, 49119 plasmapause locations are identified from the in-situ observations and 3957 plasmapause profiles (corresponding to 48899 plasmapause locations in 1 h MLT intervals) are extracted from the EUV images. Since the plasmapause crossings of all the satellites are not all located in the SM equator, the IGRF internal magnetic field model combined with the Tsyganenko 2007 external magnetic field model are used to map the crossings to the SM equator, and the corresponding UT, L value (L_{PP}) and MLT are stored into a database. Then, all the crossings in the database are matched with the geomagnetic indices of 3-hour *Kp*, 1-hour *Dst*, 5-minute *SYM-H*, and 5-minute *AE*, as well as the 5-minute averaged solar wind speed (V_{SW}), solar wind number density (N_{SW}), y component of IMF (IMF B_{Y}), and z component of IMF (IMF B_{Z}). The *Dst*, *SYM-H* and *AE* indices are provided by the Kyoto World Data Center for Geomagnetism, the *Kp* index is provided by the German Research Centre for Geosciences (GFZ), and the solar wind data are obtained from the NASA's CDAWEB OMNI.

In matching the solar wind and IMF parameters, since the OMNI data have been time shifted to the nose of the Earth's bow shock, here we just consider the propagation of the solar wind from the bow shock nose to the high latitude polar region. According to *Zhang et al.* [2005], the time shift includes two parts. The first part is the time delay (τ_{mp}) from the bow shock to the subsolar magnetopause using the average shocked solar wind velocity (V_{SWX}) with a reduction factor of 8. The second part is the estimated time (τ_{Alfven}) of Alfvénic perturbation propagating from the subsolar magnetopause to the Earth's high latitude region. The bow shock position X_{BS} is calculated from the *Chao et al.* [2002] bow shock model, and the subsolar magnetopause position X_{MP} is obtained by the *Lin et al.* [2010] magnetopause model. The total time shift, T_{shift}, can be written as

$$\begin{aligned} T_{\mathrm{shift}} &= \tau_{\mathrm{mp}} + \tau_{\mathrm{Alfven}}, \\ \tau_{\mathrm{mp}} &= \frac{X_{\mathrm{BS}} - X_{\mathrm{MP}}}{V_{\mathrm{SWX}}} \times 8, \\ \tau_{\mathrm{Alfven}} &= 2.0 \text{ min.} \end{aligned} \qquad (2)$$

Since the 5-min averaged OMNI data are available only after 1995, only the plasmapause locations observed after 1995 are matched with the shifted solar wind and IMF parameters.

2.6. Overview of Database

The histograms of the number of plasmapause locations versus UT, month, MLT and year are shown in Figure 7. There are more than 3000 events in each 1-hour UT bin and more than 4000 events in each month, as shown in Figure 7*a* and 7*b*, respectively. It is shown in Figure 7*c* that there are more than 2000 events in each 1-hour MLT bin, providing statistical confidence for establishment of an empirical plasmapause model with MLT-dependence. The event numbers in each year are shown in Figure 7*d*. Due to the low plasmaspheric crossing frequency of ISEE-1, the yearly event number is small before 1987 (except for 1981-1984 when DE-1 data were available) compared with other satellites after 1990. No plasmaspheric observation is found in 1988 (based on our knowledge).

The MLT distributions of the plasmapause locations versus various parameters are shown in Figure 8. Figure 8*a* reveals that most of the plasmapause locations are observed between 3.0 R_E and 6.0 R_E. A clear bulge structure is shown in Figure 8*a* in the dusk sector as demonstrated by the gray dotted curve. Figures 8*b*-8*d* indicate that most of the plasmapause locations are observed during periods of quiet or slightly disturbed geomagnetic conditions, with average *Kp* index of ~3.0, average *Dst* index of ~-20 nT, and average *AE* index of ~250 nT, respectively. For the IMF conditions, B_Y and B_Z for most of the plasmapause locations are between -10.0 and 10.0 nT with average values of B_Y around 0.0 nT and B_Z around -1.0 nT as shown in Figures 8*e* and 8*f*, respectively. Figures 8*g* and 8*h* demonstrate that most of the plasmapause locations are observed when V_{SW} is less than 600 km/s and N_{SW} is less than 12.0 cm^{-3} with average values of ~450 km/s and ~6.0 cm^{-3}, respectively.

3. Variations of Plasmapause Locations

Based on the large database covering almost four solar cycles with sufficient sampling of the geomagnetic indices and solar wind and IMF parameters, we could more thoroughly investigate the global shape variations and the MLT-dependent diurnal, seasonal and solar cycle variations of the plasmapause locations.

3.1. Variations of Global Shape

Figure 9 shows global shapes of the plasmapause under different geomagnetic, solar wind and IMF conditions. The dotted curves are binned in 1 h MLT intervals. *Black*, *blue*, *purple*, and *red* lines represent different levels of activity, typically (but not always) lowest to highest, respectively, as demonstrated at the bottom of each panel. In Figure 9, the IMF clock angle θ is defined by θ = atan($|B_Y|/B_Z$), with $\theta = 0°$ for northward IMF and $\theta = 180°$ for southward IMF. In addition, the solar cycle phase (minimum, ascending, maximum, and descending for the four colors, respectively) is determined by the value and time sequence of F10.7A, which is the yearly average of the daily F10.7 values. It needs to be noted that F10.7A must be greater than the previous year's average for the ascending solar cycle phase, while F10.7A must be less than the previous year's average for the descending solar cycle phase.

The *t*-test [*Press et al.*, 1992] shows that the average plasmapause locations at different activity levels are truly different from each other. The curves in Figures 9*a*-9*c* and 9*g* are truly different at all MLT sectors with significance levels of 100% and the significance levels are generally 95% in Figure 9*d* (except for the black-red and blue-purple comparisons in almost all MLT sectors), Figure 9*e* (except for the purple-black comparison in the 6 h – 12 h and 16 h – 20 h MLT regions and the purple-blue comparison in the 13 h – 17 h MLT range), Figure 9*f* (except for the black-blue comparison in all MLT sectors and all colors between 13 h – 16 h MLT), Figure 9*h* (except for nightside MLT sectors), and Figure 9*i* (except for the blue-black comparison in the 12 h – 18 h MLT sector).

To further quantify the uncertainties in the statistical results in Figure 9, the analysis is run for 11 times (R01–R11) for the data binned by *Kp*. R01 is set to be the baseline, in which the plasmapause data from all the 10 missions are included. In each run from R02 – R11, the plasmapause data from one mission are omitted. Here, the plasmapause data are also binned into four groups according to *Kp* levels shown in Figure 9*a* in each run. The relative errors of R02 – R11 to R01 for each *Kp* level are shown in Figure 10. It is shown that all the relative errors are less than 0.3 R_E. Based on the comparisons in section 2.4, the *t*-test above, and the multiple runs here, it is demonstrated that the database established in this investigation is credible and correct, and is suitable for statistical study of the plasmapause locations.

Based on the statistical results in Figure 9, the variations of the global shapes of the plasmapause can be summarized as follows:

1. As the geomagnetic, solar wind and IMF conditions change from quiet to disturbed, the plasmapause shrinks towards the Earth at all MLTs, except for changes in B_Y shown in Figure 9*d* and increases in N_{SW} in Figure 8*h*. Increasing N_{SW} results in the outward expansion of the plasmapause in Figure 9*h*. The possible reason for this phenomenon may be that N_{SW} is generally inversely proportional to V_{SW} [*Russell*, 2001] and the corresponding geomagnetic activity is relatively weak for large N_{SW}.

2. A significant plasmaspheric bulge is shown in the afternoon to pre-midnight MLT sector in all panels of Figure 9 under all levels of activities. The bulges are more significant under disturbed periods (purple dotted and red dotted lines). This feature is consistent with the traditional picture for large-scale plasmaspheric convection [*Chen and Wolf*, 1972; *Rasmussen et al.*, 1993]. This may also be caused by the fact that plasmaspheric plumes are observed mostly during disturbed periods, e.g., storm times or southward IMF [such as shown in *Darrouzet et al.,* 2008].
3. The shape of the plasmapause is found to be significantly different between active and quiet conditions. Generally, the differences between the storm-time (red dotted lines in Figures 9*a* and 9*b*) and non-storm-time (black dotted lines in Figures 9*a* and 9*b*) plasmapause locations can be larger than 2.5 R_E in equatorial geocentric distance and the decrease in plasmapause locations can be as large as 2.0 R_E during substorm-times (red dotted line in Figure 9*c*).
4. Orientation of the IMF can also change the plasmapause shape. The plasmapause shapes have little variation for different conditions of IMF B_Y (Figure 9*d*). The plasmapause locations move inward significantly when $B_Z < -3$ nT (Figure 8*e*). Figure 9*f* further reveals that, southward IMF (black dotted and blue dotted lines) can cause obvious shrinkage of the plasmapause which has little change during northward IMF (purple dotted and red dotted lines). Detailed correlations of the plasmapause locations with the solar wind and IMF parameters will be discussed elsewhere [*He et al.,* this issue].
5. Clear solar cycle variations are shown in Figure 9*i*. The plasmapause is the farthest from the Earth during solar minimum (black dotted line), then moves towards the Earth during the solar

ascending phase (blue dotted line) and is the closest to the Earth during solar maximum (purple dotted line) followed by an outward expansion during the solar descending phase (red dotted line).

3.2. Diurnal Variations

Figure 11 presents the diurnal variations of the plasmapause locations under geomagnetically quiet ($Kp < 4$) and disturbed ($Kp \geq 4$) conditions. It is worth recognizing that Kp = 3 to 4 represents moderately disturbed conditions and Kp alone does not discriminate between quiet and disturbed plasmaspheric distributions. Kp could be in this range, yet has most recently been in a state of prolonged quiet, prolonged activity, or prolonged variability. Each of these generalized conditions will result in distinct distributions of plasmaspheric plasma. This is a systemic limitation of all the geomagnetic indices. It is acknowledged that these interpretations of the statistical data are somewhat compromised in this way. The plasmapause locations are first binned into an MLT-UT coordinate frame in 1 h intervals and then plotted in Figure 11. The plasmapause locations in the 12 h to 21 h MLT sector are generally greater than at other MLT, consistent with the average curve in Figure 8*a*, possibly because the plasmaspheric bulges or plumes are mostly observed in the afternoon to the pre-midnight MLT sectors [*Darrouzet et al*., 2008].

Figure 11 also reveals that there is a strong correlation with UT, which represents both time and geographic longitude. This is independent of season and only loosely dependent on geomagnetic activity. The double peaks around 16 h MLT are most probably the result of the difference between the magnetic dipole tilt and the Earth’s spin axis. The North Geographic Pole is about 4.7 hours west of Greenwich. The large peaks best match that offset for quiet conditions in Figure 11*a*, but are shifted for active conditions in Figure 11*b*, both shifted toward midnight slightly. Inside of *L*-value = 4.5 R_E (~ 0 h – 9 h MLT) there is a local maximum in the plasmapause radius at two times of the day. The peak near 0 h MLT and 2 h UT shifts to later MLT faster than UT (the dashed lines indicate the shifts at the same rate of MLT and UT, that is dMLT / dUT =1.0). The other peak shifts at about the same rate in MLT and UT. The peaks near 16 h MLT also shift differently relative to UT, possibly due to the fact when the solar wind or geomagnetic condition becomes disturbed, the strong convection electric fields dominate the dynamics of the plasmasphere [*Carpenter and Park*, 1973; *Katus et al.*, 2015]. Figure 11 exhibits a statistical picture of the plasmapause azimuthal shape modulated by the magnetic dipole tilt. That how much of this display is influenced by the degree of corotation [*Sandel et al.*, 2003; *Burch et al.*, 2004; *Gallagher et al.*, 2005] and how much by geography [*Menk et al.*, 2012] needs further refined investigations.

3.3. Seasonal Variations

The seasonal variations of the plasmapause locations are shown in Figure 12. The seasonal variation of the plasmapause is characterized by obvious valleys in equinoxes and peaks in solstices in Figure 12. This seasonal variation seems to be the result of the Russell-McPherron effect [*Russell and McPherron*, 1973]. According to the Russell-McPherron effect, geomagnetic activity is strong during equinoxes and weak during solstices. The plasmapause will move towards the Earth as the geomagnetic activity changes from quiet to disturbed. Such variability of the plasmapause has been revealed in numerous observational studies [e.g., *Carpenter and Anderson*, 1992; *Sandel et al.*, 2003; *Spasojević et al.*, 2003; *He et al.*, 2016; and references therein] and modeling investigations [e.g., *Rasmussen et al.*, 1993; *Lambour et al.*, 1997; *Ober et al.*, 1997; *Liemohn et al.*, 2004].

3.4. Solar Cycle Variations

Figure 13 shows the solar cycle variation of the plasmapause locations. The plasmapause locations are first binned into a year-MLT coordinate frame in 1 year and 1 h intervals, respectively, and then plotted in Figure 13. The most important result in Figure 13 is that the plasmapause locations are strongly correlated with solar activity. The plasmapause is significantly negatively correlated to solar activity as represented by the sunspot number. The correlations before 1988 are not so significant as those after 1989, possibly because the number of plasmapause crossings in our database is small before 1988 as indicated in Figure 7. It is also interesting that the plasmapause radial position increases as the peak in solar activity falls from Solar Cycle 21 to Solar Cycle 24 as shown in the top panel of Figure 13. This implies that solar activity plays an important role in the dynamics of the plasmasphere, and the solar cycle effects should be considered in the construction of an empirical plasmapause model.

4. Summary and Conclusion

In this paper, we have compiled a large plasmapause location database, based on which the variations of the plasmapause are statistically investigated. The results are summarized as follows:

1. Based on the plasmapause identification criteria for Plasma Wave instruments and EUV images, a database that contains 49119 plasmapause crossing events from in-situ observations and 3957 plasmapause profiles (corresponding to 48899 plasmapause locations in 1 h MLT intervals)

from remote observations has been assembled, based on data from 18 satellites that cover a period from November 1977 to December 2015. To our knowledge, this is the largest plasmapause database that is so far been developed. This database also contains the matched geomagnetic indices (*Kp*, *Dst*, and *AE*) and time-shifted solar wind and IMF parameters (V_{SW}, N_{SW}, IMF B_Y and B_Z). This will be an important database for the space research community in investigating inner magnetospheric dynamics associated with other modeling and observations.

2. The responses of the global plasmapause to geomagnetic indices and solar wind changes and the diurnal, seasonal, solar cycle variations of the plasmapause are investigated based on this database. It is found that the plasmapause shrinks towards the Earth globally and a clear bulge appears in the afternoon to pre-midnight MLT sector as the solar wind and geomagnetic conditions change from quiet to disturbed. The bulges are clearer during storm times or southward IMF. For the diurnal, seasonal, and solar cycle variations, the *t*-test indicates that the peaks and valleys in Figures 11–13 are significantly different with 99% confidence levels.
3. The diurnal variations of the plasmapause azimuthal shape are most probably the result of the difference between the magnetic dipole tilt and the Earth’s spin axis.
4. The seasonal variation of the plasmapause is characterized by spring and fall valleys and summer and winter peaks.
5. The plasmapause approaches the Earth during high solar activity and expands outward during low solar activity.

Based on this large database and the above-mentioned statistical results, a new solar wind driven global dynamic plasmapause model will be constructed and validated in the companion paper [*He et al.*, this issue]. This database will also help us to better understand the evolving properties of the plasmapause shape and position as the plasmasphere interacts with the ring current and the radiation belts in the magnetosphere.

Appendix: MLA

Determination of the magnetic equatorial plane plasmapause from plasmaspheric EUV images obtained from side perspectives is challenging. The magnetic dipole nature of the plasmasphere can enable determination of the equatorial plasmapause from just one EUV image even when it is projected on the meridian plane. It is easy to understand the application of the MLA to images from polar perspectives (e.g., IMAGE EUV) since the images are approximately projected onto the magnetic equator (ME) on which the MLT-dependencies are apparently exhibited and the MLT-dependencies of the plasmapause locations can be determined [*Wang et al.*, 2007]. For side perspectives (e.g., CE-3 EUVC), as is stated in *He et al.* [2011, 2016], there are mainly two limitations in determination of the MLT-dependencies of the plasmapause shape from Moon-based images.

The first limitation is the imager-to-ME distance. Taking a plasmasphere with a uniform MLT distribution and plasmapause location at L=4.5 R_E for an example, and adopting a dipolar approximation (see Figure A1), the equation for the plasmapause shape is $r = L \times \cos^2(\theta) = 4.5 \times \cos^2(\theta)$, where θ is latitude in SM and r is the radial distance of the plasmapause at θ. The maximum distance of the plasmapause to the ME can be calculated as $z_{\mathrm{max}} = L \times \cos^2(\theta) \times \sin(\theta) = 1.73\ R_{\mathrm{E}}$. If the imager-to-ME distance is less than z_{max} (e.g., point C in the region confined by the two horizontal dashed lines in Figure A1), then the blue LOS' though pixels on the plasmasphere outline boundary in the images can only be tangent to the plasmapause surface that faces the imager with the other side shaded by the main body of the plasmasphere. For all the cases used in the investigation, the imager-to-ME distance is significantly greater than z_{max} (e.g., point A in Figure A1), so the plasmasphere outline boundary can cover all the MLT sectors. Figure A1 is just an example on the noon-midnight meridian plane. For other meridian planes, the principle is the same.

The second limitation is the shading of the main body of the plasmasphere. Due to the observing geometry from a side perspective, the plasmaspheric structures (plume, notch, shoulder, etc.) may be shaded by the main plasmasphere, and only the plasmapause of the main plasmasphere can be determined. In this investigation, only the images with clear and sharp plasmasphere outline boundaries are selected to determine the plasmapause locations on the equatorial plane in SM.

A graphical user interface (GUI) in Interactive Data Language (IDL) is prepared as supporting information Software S1 to show the feasibility of determining the MLT-dependence of the plasmapause locations from Moon-based EUV images. In the GUI, the location of the virtual imager is the same as point A in Figure A1. As pointed above, when the imager-to-ME distance is large enough, the LOS' calculated from the pixels on the plasmapause outline boundary in the images can be tangent to the plasmapause surface at all MLTs except for shading of the main plasmasphere.

Acknowledgements

The authors sincerely thank the National Astronomical Observatories, Chinese Academy of Sciences, for provision of the CE-3 EUVC data, NASA/CDAWEB for provision of the ISEE-1 PWI data, DE-1 PWI data, Polar PWI data, and IMAGE RPI data, ESA/Cluster Science Archive for provision of the Cluster WHISPER data, Iowa University for the provision of the VAP EMFISIS data available from http://emfisis.physics.uiowa.edu/data/index, the THEMIS team for provision of the THEMIS ESA and EFI data available from http://themis.ssl.berkeley.edu/index.shtml, JAXA/DARTS for provision of the Akebono PWS data, and Dr. T. Forrester of IMAGE EUV team for provision of the IMAGE EUV data and relevant processing software. The authors give thanks to NASA-CCMC for providing the code of IGRF and Tsyganenko model, NASA/GSFC OMNIWeb for providing the 5-min averaged solar wind and IMF data, the Kyoto World Data Center for providing *Dst*, *SYM-H* and *AE*, and the German Research Centre for Geosciences (GFZ) for providing *Kp*. This work was supported by the National Natural Science Foundation of China (41274147 and 41674155) and the Youth Innovation Promotion Association (No. 2017258), Chinese Academy of Sciences. Support for the US authors was provided by NASA. The newly compiled plasmapause database is available by request through email to the corresponding author.

References:

Anderson, R. R., D. A. Gurnett, and D. L. Odem (1992), CRRES plasma wave experiment, *J.*

Spacecr. Rockets, 29(4), 570-573, doi: 10.2514/3.25501.

Angelopoulos, V. (2008), The THEMIS mission, *Space Sci. Rev.*, 141, 5–34, doi:10.1007/s11214-008-9336-1.

Bandić, M., G. Verbanac, M. B. Moldwin, V. Pierrard, and G. Piredda (2016), MLT dependence in the relationship between plasmapause, solar wind, and geomagnetic activity based on CRRES: 1990–1991, *J. Geophys. Res. Space Physics*, 121, 4397–4408, doi:10.1002/2015JA022278.

Bonnell, J. W., F. S. Mozer, G. T. Delory, A. J. Hull, R. E. Ergun, C. M. Cully, V. Angelopoulos, and P. R. Harvey (2008), The Electric Field Instrument (EFI) for THEMIS, *Space Sci. Rev.*, 141, 303–341, doi:10.1007/s11214-008-9469-2.

Burch, J. L. (2000), IMAGE mission overview, *Space Sci. Rev.*, 91(1), 1-14, doi: 10.1023/A:1005245323115.

Burch, J. L., J. Goldstein, and B. R. Sandel (2004), Cause of plasmasphere corotation lag, *Geophys. Res. Lett.*, 31, L05802, doi:10.1029/2003GL019164.

Carpenter, D. L. (1963), Whistler evidence of a ‘Knee’ in the magnetospheric ionization density profile, *J. Geophys. Res.*, 68(6), 1675-1682, doi:10.1029/ JZ068i006p01675.

Carpenter, D. L. (1966), Whistler studies of the plasmapause in the magnetosphere: 1. Temporal variations in the position of the knee and some evidence on plasma motions near the knee, J. Geophys. Res., 71(3), 693–709, doi:10.1029/JZ071i003p00693.

Carpenter, D. L. (1995), Earth’s plasmasphere awaits rediscovery, *Eos Trans. AGU*, 76(9), 89-92, doi: 10.1029/95EO00041.

Carpenter, D. L. (2004), Remote sensing the Earth's plasmasphere, *Rad. Sci. Bull.*, 308, 13-29.

Carpenter, D. L., and R. R. Anderson (1992), An ISEE/whistler Model of Equatorial Electron Density in the Magnetosphere, *J. Geophys. Res.*, 97(A2), 1097-1108, doi: 10.1029/91JA01548.

Carpenter, L. D., and C. Park (1973), On what ionospheric workers should know about the plasmapause-plasmasphere, *Rev. Geophys. Space Phys.*, 11, 133–154.

Chao, J. K., D. J. Wu, C.‐H. Lin, Y. H. Yang, X. Y. Wang, M. Kessel, S. H. Chen, and R. P. Lepping (2002), Models for the size and shape of the Earth's magnetopause and bow shock, in *Space Weather Study Using Multipoint Techniques, COSPAR Colloq. Ser.*, vol. 12, edited by L.-H. Lyu, pp. 127‐134, Pergamon, Oxford.

Chappell, C. R., K. K. Harris, and G. W. Sharp (1970), A study of the influence of magnetic activity on the location of the plasmapause as measured by OGO 5, *J. Geophys. Res.*, 75(1), 50-56, doi: 10.1029/JA075i001p00050.

Chen, B., et al. (2014), Investigation and calibration of the Moon-based EUV camera for Chang'E-3, *Res. Astron. Astrophys.*, 14(12), 1654–1663, doi:10.1088/1674-4527/14/12/013.

Chen, A. J., and R. A. Wolf (1972), Effects on the plasmasphere of a time varying convection electric field, *Planet. Space Sci.*, 20(4), 483–509, doi:10.1016/0032-0633(72)90080-3.

Cho, J., D.-Y. Lee, J.-H. Kim, D.-K. Shin, K.-C. Kim, and D. Turner (2015), New model fit functions of the plasmapause location determined using THEMIS observations during the ascending phase of Solar Cycle 24, *J. Geophys. Res. Space Physics*, 120, 2877–2889, doi:10.1002/2015JA021030.

Comfort, R. H., J. H. Waite Jr., and C. R. Chappell (1985), Thermal ion temperatures from the retarding ion mass spectrometer on DE 1, *J. Geophys. Res.*, 90(A4), 3475–3486, doi:10.1029/JA090iA04p03475.

Darrouzet, F., P. M. E. Décréau, and J. Lemaire (2002), The Cluster mission preliminary results obtained with the WHISPER experiment, *Physicalia Mag.*, 24, 3-16, doi: 10.1.1.568.6231.

Darrouzet, F., P. M. E. Décréau, J. De Keyser, A. Masson, D. L. Gallagher, O. Santolik, B. R. Sandel, J. G. Trotignon, J. L. Rauch, E. Le Guirriec, P. Canu, F. Sedgemore, A. André, and J. F. Lemaire (2004), Density structures inside the plasmasphere: Cluster observations, *Ann. Geophys*., 22, 2577-2585, doi: 10.5194/angeo-22-2577-2004.

Darrouzet, F., J. De Keyser, P. M. E. Décréau, F. El Lemdani-Mazouz, and X. Vallières (2008), Statistical analysis of plasmaspheric plumes with Cluster/WHISPER observations, *Ann. Geophys.*, 26, 2403-2417, doi: 10.5194/angeo-26-2403-2008.

Darrouzet, F., De Keyser, J., and Pierrard, V. (Eds.) (2009), *The Earth's Plasmasphere: A Cluster and IMAGE Perspective*, Springer, New York, U.S.A., doi:10.1007/978-1-4419-1323-4.

Darrouzet, F., V. Pierrard, S. Benck, G. Lointier, J. Cabrera, K. Borremans, N. Y. Ganushkina, and J. De Keyser (2013), Links between the plasmapause and the radiation belt boundaries as observed by the instruments CIS, RAPID and WHISPER onboard Cluster, *J. Geophys. Res. Space Physics*, 118, 4176–4188, doi:10.1002/jgra.50239.

Décréau, P. M. E., P. Fergeau, V. Krannosels'kikh, M. Lévêque, Ph. Martin, O. Randriamboarison, F. X. Sené, J. G. Trotignon, P. Canu, P. B. Mögensen (1997), WHISPER, a resonance sounder and wave analyser: Performances and perspectives for the Cluster mission, *Space Sci. Rev.*, 79, 157:193, doi: 10.1023/A:1004931326404.

Fok, M.-C., T. E. Moore, J. U. Kozyra, G. C. Ho, and D. C. Hamilton (1995), Three-dimensional ring current decay model, *J. Geophys. Res.*, 100(A6), 9619–9632, doi:10.1029/94JA03029.

Gallagher, D. L., M. L. Adrian, and M. W. Liemohn (2005), Origin and evolution of deep plasmaspheric notches, *J. Geophys. Res.*, 110, A09201, doi:10.1029/2004JA010906.

Gallagher, D. L., and R. H. Comfort (2016), Unsolved problems in plasmasphere refilling, *J. Geophys. Res. Space Physics*, 121, 1447–1451, doi:10.1002/2015JA022279.

Ganguli, G., M. A. Reynolds, and M. W. Liemohn (2000), The plasmasphere and advances in plasmaspheric research, *J. Atmos Sol.-Terr. Phys.*, 62(17-18), 1647-1657, doi: 10.1016/S1364-6826(00)00117-6.

Goldstein, J., M. Spasojevic, P. H. Reiff, B. R. Sandel, W. T. Forrester, D. L. Gallagher, and B. W. Reinisch (2003a), Identifying the plasmapause in IMAGE EUV data using IMAGE RPI in situ steep density gradients, *J. Geophys. Res.*, 108(A4), 1147, doi:10.1029/2002JA009475.

Goldstein, J., B. R. Sandel, W. T. Forrester, and P. H. Reiff (2003b), IMF-driven plasmasphere erosion of 10 July 2000, *Geophys. Res. Lett.*, 30(3), 1146, doi:10.1029/2002GL016478.

Goldstein, J., B. R. Sandel, W. T. Forrester, M. F. Thomsen, and M. R. Hairston (2005), Global plasmasphere evolution 22–23 April 2001, *J. Geophys. Res.*, 110, A12218, doi:10.1029/2005JA011282.

Goldstein, J. (2006), Plasmasphere response: Tutorial and review of recent imaging results, *Space*

Sci. Rev., 124, 203–216, doi:10.1007/s11214-006-9105-y.

Goldstein, J., S. De Pascuale, C. Kletzing, W. Kurth, K. J. Genestreti, R. M. Skoug, B. A. Larsen, L. M. Kistler, C. Mouikis, and H. Spence (2014), Simulation of Van Allen Probes plasmapause encounters, J. Geophys. Res. Space Physics, 119, doi:10.1002/2014JA020252.

Grebowsky, J. M. (1970), Model study of plasmapause motion. *J. Geophys. Res.* 75, 4329-4333, doi: 10.1029/JA075i022p04329.

Gringauz, K. I. (1963), The structure of the ionized gas envelope of earth from direct measurements in the USSR of local charged particle concentrations, *Planet. Space Sci.*, 11(3), 281-296, doi: 10.1016/0032-0633(63)90030-8.

Gurnett, D. A., F. L. Scarf, R. W. Fredricks, and E. J. Smith (1978), The ISEE-1 and ISEE-2 plasma wave investigation, *Trans. IEEE Geosci. Electron.*, GE-16(3), 225-230, doi: 10.1109/TGE.1978.294552.

Gurnett, D. A., and U. S. Inan (1988), Plasma wave observations with the Dynamics Explorer 1 spacecraft, *Rev. Geophys.*, 26(2), 285-316, doi: 10.1029/RG026i002p00285.

Gurnett, D. A., A. M. Persoon, R. F. Randall, D. L. Odem, S. L. Remington, T. F. Averkamp, M. M. Debower, G. B. Hospodarsky, R. L. Huff, D. L. Kirchner, M. A. Mitchell, B. T. Pham, J. R. Phillips, W. J. Schintler, P. Sheyko, and D. R. Tomash (1995), The Polar plasma wave instrument, *Space Sci. Rev.*, 71(1), 597-622, doi: 10.1007/BF00751343.

Harris, K. K., and G. W. Sharp (1969), OGO-V ion spectrometer, *Trans. IEEE Geosci. Electron.*, GE-7(2), 93-98, doi: 10.1109/TGE.1969.271328.

Harris, K. K., G. W. Sharp, and C. R. Chappell (1970), Observations of the plasmapause from OGO 5, *J. Geophys. Res.*, 75(1), 219-224, doi: 10.1029/JA075i001p00219.

Harvey, P., F. S. Mozer, D. Pankow, J. Wygant, N. C. Maynard, H. Singer, W. Sullivan, P. B. Anderson, R. Pfaff, T. Aggson, A. Pedersen, C.-G. Fälthammar, and P. Tanskannen (1995), The electric field instrument on the Polar satellite, *Space Sci. Rev.*, 71, 583-596, doi:10.1007/BF00751342.

He, F., X. X. Zhang, B. Chen, and M.-C. Fok (2011), Reconstruction of the plasmasphere from Moon-based EUV images, *J. Geophys. Res.*, 116, A11203, doi:10.1029/2010JA016364.

He, F., X. X. Zhang, B. Chen, and M.-C. Fok (2012), Inversion of the Earth's plasmaspheric density distribution from EUV images with genetic algorithm, *Chinese J. Geophys.*, 55(1), 29−35, doi: 10.6038/j.issn.0001-5733.2012.01.003.

He, F., X.-X. Zhang, B. Chen, M.-C. Fok, and S. Nakano (2016), Determination of the Earth's plasmapause location from the CE-3 EUVC images, *J. Geophys. Res. Space Physics*, 121, 296–304, doi:10.1002/2015JA021863.

Horwitz, J. L., R. H. Comfort, and C. R. Chappell (1990), A statistical characterization of plasmasphere structure and boundary locations [J]. *J. Geophys. Res.*, 95, 7937-7947, doi: 10.1029/JA095iA06p07937.

Katus, R.M., D. L. Gallagher, M.W. Liemohn, A. M. Keesee, and L. K. Sarno-Smith (2015), Statistical storm time examination of MLT-dependent plasmapause location derived from IMAGE EUV, *J. Geophys. Res. Space Physics*, 120, 5545–5559, doi:10.1002/2015JA021225.

Khazanov, G. V., and M. W. Liemohn (1995), Nonsteady state ionosphere-plasmasphere coupling of superthermal electrons, *J. Geophys. Res.*, 100(A6), 9669–9681, doi:10.1029/95JA00526.

Kim, K.-H., F. S. Mozer, D.-H. Lee, and H. Jin (2010), Large electric field at the nightside plasmapause observed by the Polar spacecraft, *J. Geophys. Res.*, 115, A07219, doi:10.1029/2010JA015439.

Kletzing, C. A., W. S. Kurth, M. Acuna, R. J. MacDowall, R. B. Torbert, T. Averkamp, D. Bodet, S. R. Bounds, M. Chutter, J. Connerney, D. Crawford, J. S. Dolan, R. Dvorsky, G. B. Hospodarsky, J. Howard, V. Jordanova, R. A. Johnson, D. L. Kirchner, B. Mokrzycki, G. Needell, J. Odom, D. Mark, R. PfaffJr., J. R. Phillips, C. W. Piker, S. L. Remington, D. Rowland, O. Santolik, R. Schnurr, D. Sheppard, C. W. Smith, R. M. Thorne, J. Tyler (2013), The Electric and Magnetic Field Instrument Suite and Integrated Science (EMFISIS) on RBSP, *Space Sci. Rev.*, 179, 127–181, doi:10.1007/s11214-013-9993-6.

Kurth, W. S., S. De Pascuale, J. B. Faden, C. A. Kletzing, G. B. Hospodarsky, S. Thaller, and J. R. Wygant (2015), Electron densities inferred from plasma wave spectra obtained by the Waves instrument on Van Allen Probes, *J. Geophys. Res. Space Physics*, 120, 904–914, doi:10.1002/2014JA020857.

Kwon, H.-J., K.-H. Kim, G. Jee, J.-S. Park, H. Jin, and Y. Nishimura (2015), Plasmapause location under quiet geomagnetic conditions (Kp ⩽ 1): THEMIS observations, *Geophys. Res. Lett.*, 42, 7303–7310, doi:10.1002/2015GL066090.

Lambour, R. L., L. A. Weiss, R. C. Elphic, and M. F. Thomsen (1997), Global modeling of the plasmasphere following storm sudden commencements, *J. Geophys. Res.*, 102(A11), 24351–24368, doi:10.1029/97JA02037.

Larsen, B. A., D. M. Klumpar, and C. Gurgiolo (2007), Correlation between plasmapause position and solar wind parameter, *J. Atmos. Sol. Terr. Phys.*, 69, 334–340, doi:10.1016/j.jastp.2006.06.017.

Lawrence, D. J., M. F. Thomsen, J. E. Borovsky, and D. J. McComas (1999), Measurements of early and late time plasmaspheric refilling as observed from geosynchronous orbit, *J. Geophys. Res.*, 104, 14,691-14,704, doi:10.1029/1998JA900087.

Lemaire, J. F., and K. I. Gringauz (1998), *The Earth's Plasmasphere*, with contributions from D. L. Carpenter and V. Bassolo, 372 pp., Cambridge Univ. Press, New York, doi:10.1017/CBO9780511600098.

Li, W., R. M. Thorne, J. Bortnik, Y. Nishimura, V. Angelopoulos, L. Chen, J. P. McFadden, and J. W. Bonnell (2010), Global distributions of suprathermal electrons observed on THEMIS and potential mechanisms for access into the plasmasphere, *J. Geophys. Res.*, 115, A00J10, doi:10.1029/2010JA015687.

Liemohn, M. W., A. J. Ridley, D. L. Gallagher, D. M. Ober, and J. U. Kozyra (2004), Dependence of plasmaspheric morphology on the electric field description during the recovery phase of the 17 April 2002 magnetic storm, *J. Geophys. Res.*, 109, A03209, doi:10.1029/2003JA010304.

Liemohn, M. W. (2006), Introduction to the special section on "Results of the National Science Foundation Geospace Environment Modeling Inner Magnetosphere/Storms Assessment Challenge" *J. Geophys. Res.*, 111. A11S01, doi: 10.1029/2006JA011970.

Lin, R. L., X. X. Zhang, S. Q. Liu, Y. L. Wang, and J. C. Gong (2010), A three-dimensional asymmetric magnetopause model, *J. Geophys. Res.*, 115, A04207, doi:10.1029/2009JA014235.

Liu, X., W. Liu, J. B. Cao, H. S. Fu, J. Yu, and X. Li (2015), Dynamic plasmapause model based on THEMIS measurements, *J. Geophys. Res. Space Physics*, 120, 10,543–10,556, doi:10.1002/2015JA021801.

McFadden, J. P., C. W. Carlson, D. Larson, M. Ludlam, R. Abiad, B. Elliott, P. Turin, M. Marckwordt, and V. Angelopoulos (2008), The THEMIS ESA plasma instrument and in-flight calibration, *Space Sci. Rev.*, 141, 277–302, doi:10.1007/s11214-008-9440-2.

Menk, F. W., S. T. Ables, R. S. Grew, M. A. Clilverd, and B. R. Sandel (2012), The annual and longitudinal variations in plasmaspheric ion density, *J. Geophys. Res.*, 117, A03215, doi:10.1029/2011JA017071.

Moldwin, M. B., M. F. Thomsen, S. J. Bame, D. J. McComas, and G. D. Reeves (1995), The fine-scale structure of the outer plasmasphere, *J. Geophys. Res.*, 100, 8021-8029, doi:10.1029/94JA03342.

Moldwin, M. B., L. Downward, H. K. Rassoul, R. Amin, and R. R. Anderson (2002), A new model of the location of the plasmapause: CRRES results, *J. Geophys. Res.*, 107(A11), 1339, doi:10.1029/2001JA009211.

Mozer, F. S. (1973), Analyses of techniques for measuring DC and AC electric fields in the magnetosphere, *Space Sci. Rev.*, 14(2), 272–313, doi:10.1007/BF02432099.

Newberry, I. T., R. H. Comfort, P. G. Richards, and C. R. Chappell (1989), Thermal He+ in the plasmasphere: Comparison of observations with numerical calculations, *J. Geophys. Res.*, 94(A11), 15265–15276, doi:10.1029/JA094iA11p15265.

Ober, D. M., J. L. Horwitz, and D. L. Gallagher (1997), Formation of density troughs embedded in the outer plasmasphere by subauroral ion drift events, *J. Geophys. Res.*, 102, 14,595–14,602, doi:10.1029/97JA01046.

O'Brien, T. P., and M. B. Moldwin (2003), Empirical plasmapause models from magnetic indices, *Geophys. Res. Lett.*, 30(4), 1152, doi:10.1029/2002GL016007.

Ogilvie, K. W., T. von Rosenvinge, and A. C. Durgey (1977), International Sun-Earth Explorer: A three-spacecraft program, *Science*, 198 (4313), 131-138, doi: 10.1126/science.198.4313.131.

Olsen, R. C., S. D. Shawhan, D. L. Gallagher, J. L. Green, C. R. Chappell, and R. R. Anderson (1987), Plasma observations at the Earth's magnetic equator, *J. Geophys. Res.*, 92(A3), 2385–2407, doi:10.1029/JA092iA03p02385.

Oya, H., A. Morioka, K. Kobayashi, M. Iizima, T. Ono, H. Miyaoka, T. Okada, and T. Obara (1990), Plasma wave observation and sounder experiments (PWS) using the Akebono (EXOS-D) satellite – Instrumentation and initial results including discovery of the high altitude equatorial plasma turbulence, *J. Geomag. Geoelectr.*, 42, 411-442, doi: 10.5636/jgg.42.411.

Pedersen, A., F. Mozer, and G. Gustafsson (1998), Electric field measurements in a tenuous plasma with spherical double probes, in *Measurement Techniques in Space Plasmas: Fields, Geophys. Monogr. Ser.*, vol. 103, edited by R. F. Pfaff, J. E. Borovsky, and D. T. Young, pp. 1–12, AGU, Washington, D. C.

Pierrard, V., J. Goldstein, N. André, V. K. Jordanova, G. A. Kotova, J. F. Lemaire, M. W. Liemohn, and H. Matsui (2009), Recent progress in physics-based models of the plasmasphere, *Space Sci. Rev.*, 145, 193-229, doi: 10.1007/s11214-008-9480-7.

Rasmussen, C. E., S. M. Guitar, and S. G. Thomas (1993), A two-dimensional model of the plasmasphere: Refilling time constant, *Planet. Space Sci.*, 41(1), 35–43, doi: 10.1016/0032-0633(93)90015-T.

Reinisch, B. W., D. M. Haines, K. Bibl, G. Cheney, I. A. Galkin, X. Huang, S. H. Myers, G. S. Sales, R. F. Benson, S. F. Fung, J. L. Green, S. Boardsen, W. W. L. Taylor, J.-L. Bougeret, R. Manning, N. Meyer-Vernet, M. Moncuquet, D. L. Carpenter, D. L. Gallagher, P. Reiff (2000), The Radio Plasma Imager investigation on the image spacecraft, *Space Sci. Rev.*, 91(1), 319–359, doi: 10.1023/A:1005252602159.

Press, W. H., S. A. Teukolsky, W. T. Vetterling, and B. P. Flannery (1992), *Numerical Recipes*, Cambridge Univ. Press, Cambridge, U. K.

Russell, C. T. (2001), Solar Wind and Interplanetary Magnetic Field: A Tutorial, in *Space Weather* (eds P. Song, H. J. Singer and G. L. Siscoe), American Geophysical Union, Washington, D. C.. doi: 10.1029/GM125p0073.

Russell, C. T., and R. L. McPherron (1973), Semiannual variation of geomagnetic activity, *J. Geophys. Res.*, 78(1), 92–108, doi:10.1029/JA078i001p00092.

Roelof, E. C., and A. J. Skinner (2000), Extraction of ion distributions from magnetospheric ENA and EUV images, *Space Sci. Rev.*, 91, 437-459, doi: 10.1007/978-94-011-4233-5_15.

Sandel, B. R., et al. (2000), The extreme ultraviolet imager investigation for the image mission, *Space Sci. Rev.*, 91(1), 197–242, doi:10.1023/A:1005263510820.

Sandel, B. R., J. Goldstein, D. L. Gallagher, and M. Spasojević (2003), Extreme ultraviolet imager observations of the structure and dynamics of the plasmasphere, *Space Sci. Rev.*, 109(1), 25–46, doi:10.1023/B:SPAC.0000007511.47727.5b.

Sarno-Smith, L. K., M. W. Liemohn, R. M. Skoug, B. A. Larsen, M. B. Moldwin, R. M. Katus, and J. R. Wygant (2016), Local time variations of high-energy plasmaspheric ion pitch angle distributions, *J. Geophys. Res. Space Physics*, 121, 6234-6244, doi: 10.1002/2015JA022301.

Scudder, J. D., X. Cao, and F. S. Mozer (2000), Photoemission current-spacecraft voltage relation: Key to routine, quantitative low-energy plasma measurements, *J. Geophys. Res.*, 105, 21,281-21,294, doi:10.1029/1999JA900423.

Shawhan, S. D., D. A. Gurnett, D. L. Odem, R. A. Helliwell, and C. G. Park (1981), The plasma wave and quasi-static electric field instrument (PWI) for Dynamics Explorer-A, *Space Sci. Instrum.*, 5, 535-550.

Sitnov, M. I., N. A. Tsyganenko, A. Y. Ukhorskiy, and P. C. Brandt (2008), Dynamical data-based modeling of the storm-time geomagnetic field with enhanced spatial resolution, *J. Geophys. Res.*, 113, A07218, doi:10.1029/2007JA013003.

Spasojević, M., J. Goldstein, D. L. Carpenter, U. S. Inan, B. R. Sandel, M. B. Moldwin, and B. W. Reinisch (2003), Global response of the plasmasphere to a geomagnetic disturbance, *J. Geophys. Res.*, 108(A9), 1340, doi:10.1029/2003JA009987.

Tsuruda, K., and H. Oya (1991), Introduction to the EXOS-D (Akebono) project, *Geophys. Res. Lett.*, 18(2), 2930295, doi: 10.1029/91GL00039.

Tsyganenko, N. A., and M. I. Sitnov (2007), Magnetospheric configurations from a high-resolution data-based magnetic field model, *J. Geophys. Res*., 112, A06225, doi:10.1029/2007JA012260.

Verbanac, G., V. Pierrard, M. Bandić, F. Darrouzet, J.-L. Rauch, and P. M. E. Décréau (2015), The relationship between plasmapause, solar wind and geomagnetic activity between 2007 and 2011, *Ann. Geophys.*, 33, 1271-1283, doi:10.5194/angeo-33-1271-2015.

Wang, C., T. S. Newman, and D. L. Gallagher (2006), Synthesis of 3D model of a magnetic field-influenced body from a single image, in *Proc. Third International Symposium on 3D Data Processing, Visualization and Transmission*, IEEE, Chapel Hill, N. C., pp. 1018-1025, doi: 10.1109/3DPVT.2006.133.

Wang, C., T. S. Newman, and D. L. Gallagher (2007), Plasmapause equatorial shape determination via the Minimum L algorithm: Description and evaluation, *J. Geophys. Res.*, 112, A12201, doi:10.1029/2006JA012202.

Yoshikawa, I., et al. (2008), Telescope of extreme ultraviolet (TEX) onboard SELENE: Science from the Moon, *Earth Planets Space*, 60(4), 407–416, doi:10.1186/BF03352805.

Zhang, X. X., C. Wang, T. Chen, Y. L. Wang, A. Tan, T. S. Wu, G. A. Germany, and W. Wang (2005), Global patterns of Joule heating in the high-latitude ionosphere, *J. Geophys. Res.*, 110, A12208, doi:10.1029/2005JA011222.

Tables:

Table 1. Satellite Instruments and Data Intervals Used to Extract the Plasmapause Locations

Satellites	Events Number	Instruments	Data Interval
ISEE-1	1080	PWI	13 November 1977 to 21 September 1987
DE-1	1205	PWI	16 September 1981 to 20 June 1984
Akebono	11104	PWS	05 March 1989 to 30 August 1998
CRRES	1165	PWE	01 August 1990 to 10 November 1991
Polar	7223	PWI, EFI [b]	16 March 1996 to 19 December 2006
IMAGE	2584	RPI	01 January 2001 to 18 December 2005
IMAGE	3579 [a]	EUV	13 May 2000 to 31 December 2002
Cluster (1, 2, 3, 4)	6955	WHISPER	02 February 2002 to 31 December 2012
THEMIS (A, D, E)	12024	EFI, ESA	01 January 2008 to 31 December 2015
THEMIS-B	177	EFI, ESA	02 July 2008 to 02 December 2009
THEMIS-C	602	EFI, ESA	30 June 2008 to 24 March 2010
VAP (A, B)	5000	EMFISIS	01 September 2012 to 31 December 2015
CE-3	378[a]	EUVC	24 December 2013 to 21 April 2014

[a] These values represent the number of EUV or EUVC images, respectively. Each EUV image corresponds to a plasmapause profile with 1 h MLT intervals with full MLT-coverage not guaranteed.

[b] The data coverage for PWI is from 02 February 1996 to 16 September 1997, and the data coverage for EFI is from 20 March 1996 to 28 April 2008. For the period before 16 September 1997, the PWI data are used to determine the plasmapause, and the EFI data are used for period after then. Only data before 2006 are used.

Figures and Captions:

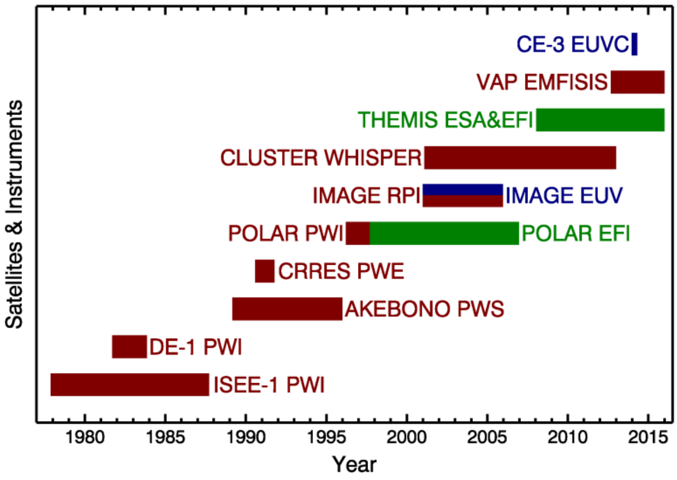

Figure 1. Coverages and overlap of satellite data used in this paper. The plasmaspheric observing instruments onboard these satellites can be divided into three categories of plasma wave instruments (red), optical remote sensing instruments (blue), and electro-static analyzers (green).

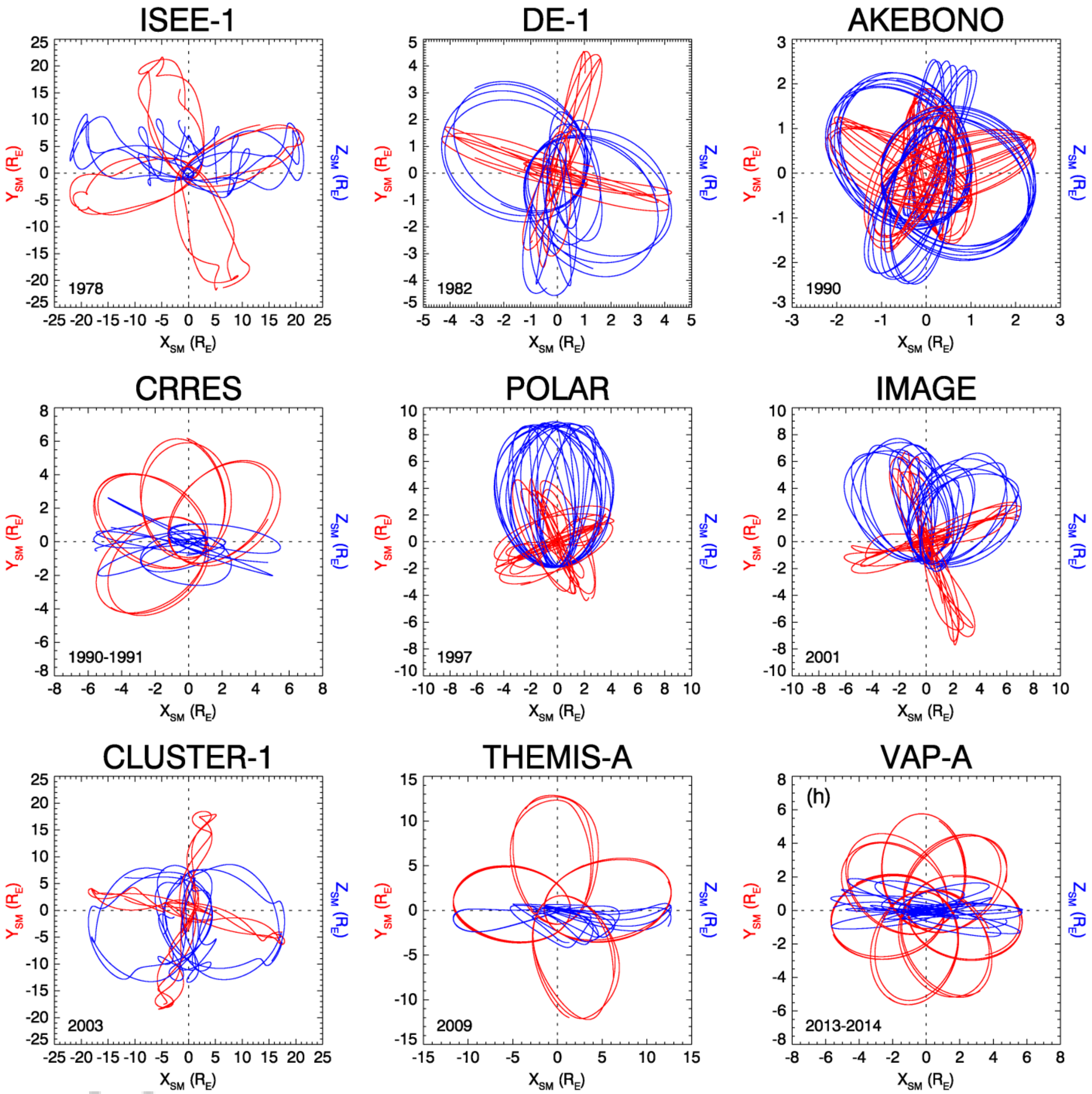

Figure 2. Sampled orbits of the nine Earth-orbiting satellites in the *xy* plane (red curves) and *xz* plane (blue curves) in the SM coordinate system. For multi-satellite missions of Cluster (four satellites), THEMIS (five satellites) and VAP (two satellite), only one of each is plotted.

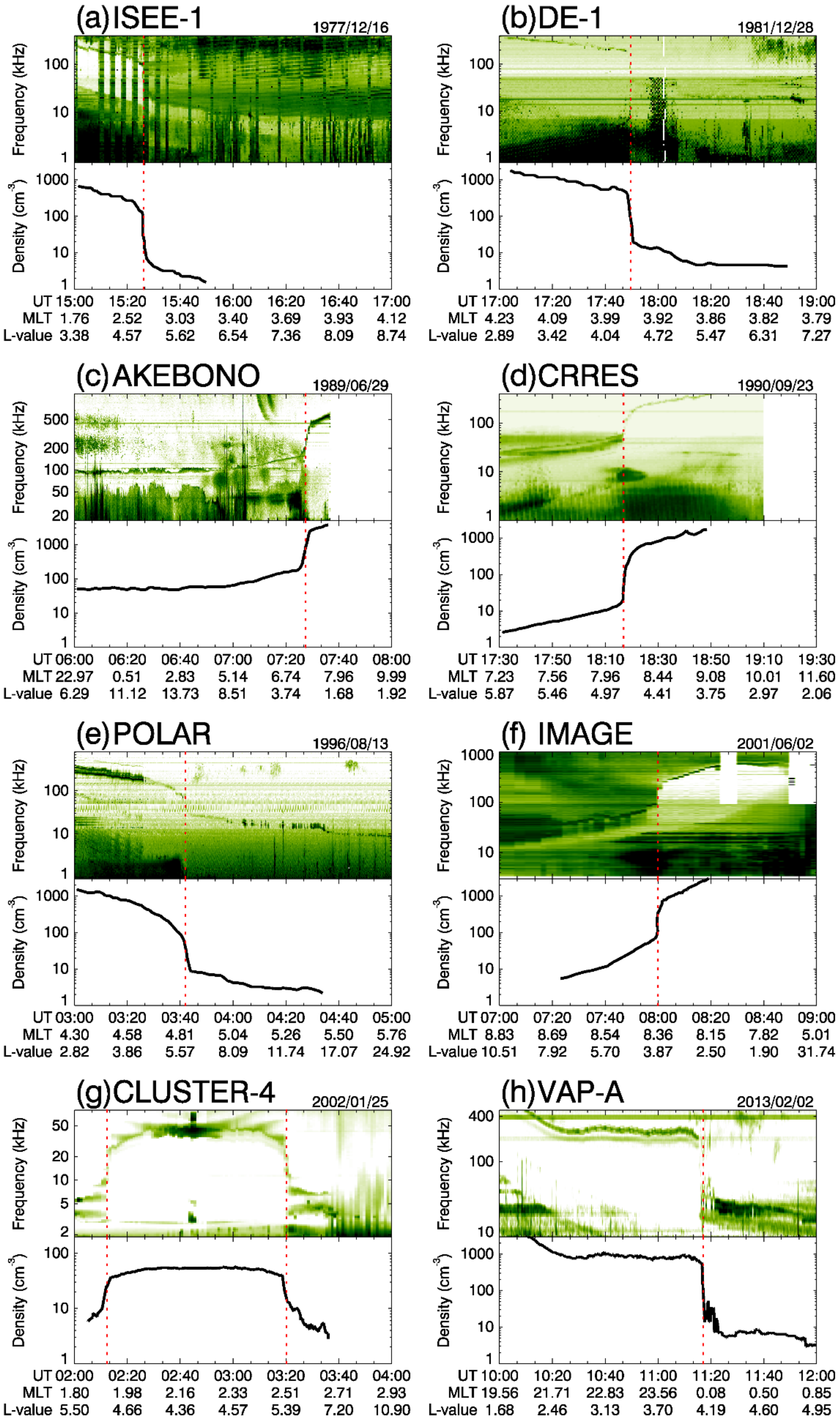
(a) ISEE-1
1977/12/16
(b) DE-1
1981/12/28
(c) AKEBONO
1989/06/29
(d) CRRES
1990/09/23
(e) POLAR
1996/08/13
(f) IMAGE
2001/06/02
(g) CLUSTER-4
2002/01/25
(h) VAP-A
2013/02/02
Frequency (kHz)
Density (cm^{-3})
UT 15:00 15:20 15:40 16:00 16:20 16:40 17:00
MLT 1.76 2.52 3.03 3.40 3.69 3.93 4.12
L-value 3.38 4.57 5.62 6.54 7.36 8.09 8.74
UT 17:00 17:20 17:40 18:00 18:20 18:40 19:00
MLT 4.23 4.09 3.99 3.92 3.86 3.82 3.79
L-value 2.89 3.42 4.04 4.72 5.47 6.31 7.27
UT 06:00 06:20 06:40 07:00 07:20 07:40 08:00
MLT 22.97 0.51 2.83 5.14 6.74 7.96 9.99
L-value 6.29 11.12 13.73 8.51 3.74 1.68 1.92
UT 17:30 17:50 18:10 18:30 18:50 19:10 19:30
MLT 7.23 7.56 7.96 8.44 9.08 10.01 11.60
L-value 5.87 5.46 4.97 4.41 3.75 2.97 2.06
UT 03:00 03:20 03:40 04:00 04:20 04:40 05:00
MLT 4.30 4.58 4.81 5.04 5.26 5.50 5.76
L-value 2.82 3.86 5.57 8.09 11.74 17.07 24.92
UT 07:00 07:20 07:40 08:00 08:20 08:40 09:00
MLT 8.83 8.69 8.54 8.36 8.15 7.82 5.01
L-value 10.51 7.92 5.70 3.87 2.50 1.90 31.74
UT 02:00 02:20 02:40 03:00 03:20 03:40 04:00
MLT 1.80 1.98 2.16 2.33 2.51 2.71 2.93
L-value 5.50 4.66 4.36 4.57 5.39 7.20 10.90
UT 10:00 10:20 10:40 11:00 11:20 11:40 12:00
MLT 19.56 21.71 22.83 23.56 0.08 0.50 0.85
L-value 1.68 2.46 3.13 3.70 4.19 4.60 4.95

Figure 3. Examples of the spectrograms of the eight plasma wave instruments showing the UHR band and plasmapause crossings. The electron densities deduced from the UHR frequencies are shown in the bottom panels. Red vertical dashed lines in each panel represent the plasmapause crossings.

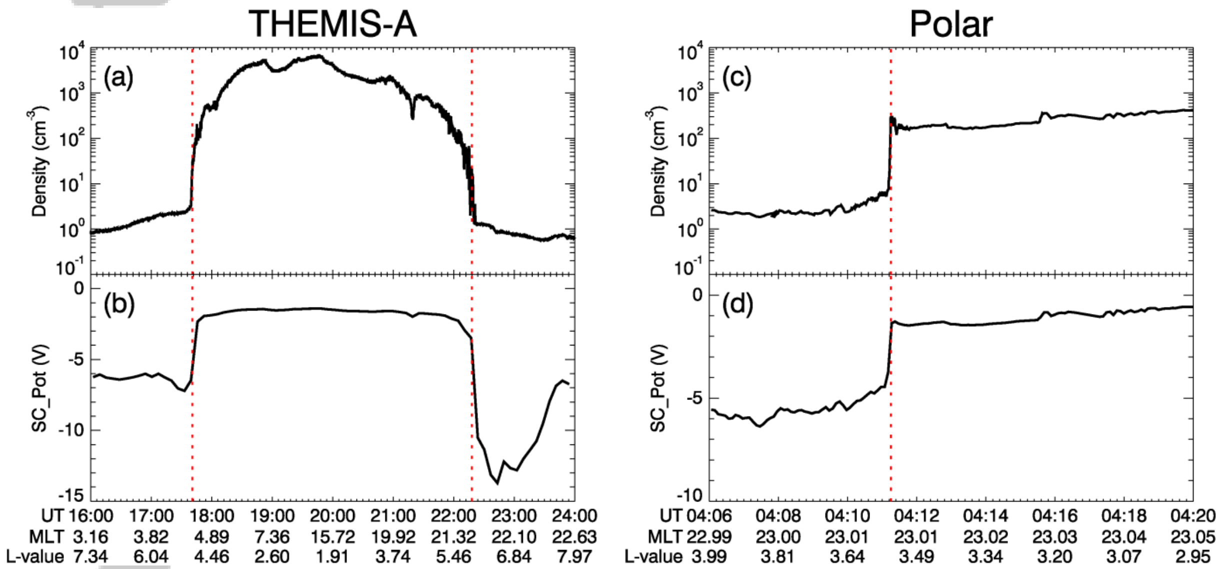

Figure 4. The spacecraft potential and electron density measured by (a-b) THEMIS-A on 31 March 2010 and (c-d) Polar on 25 April 1998, respectively. Red vertical dashed lines represent the identified plasmapause locations.

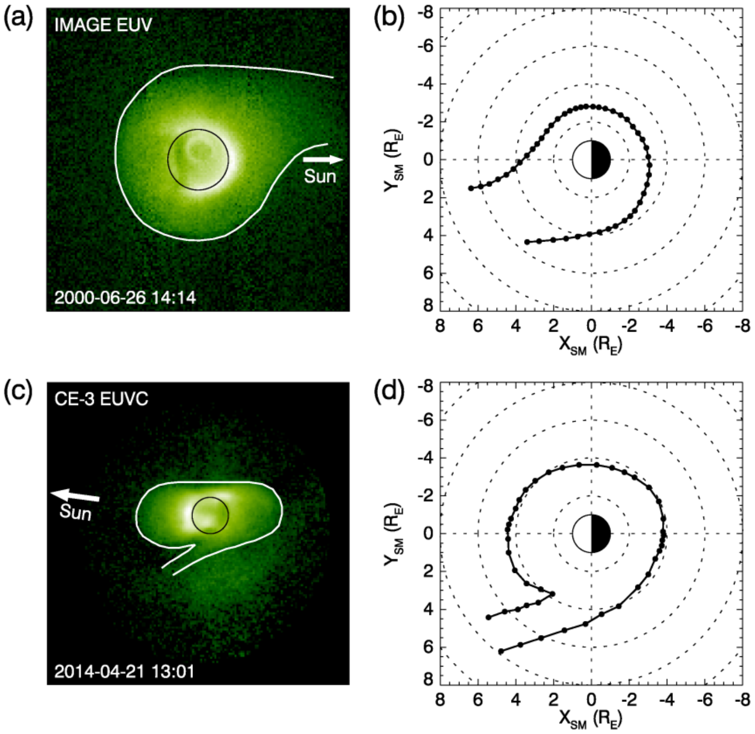

Figure 5. Examples of plasmapause determinations from EUV images. (a) and (c) are EUV images with the manually extracted plasmapause outlines shown by white curves, respectively. (b) and (d) are extracted plasmapause locations shown by solid and dotted lines from EUV images on the magnetic equator via MLA.

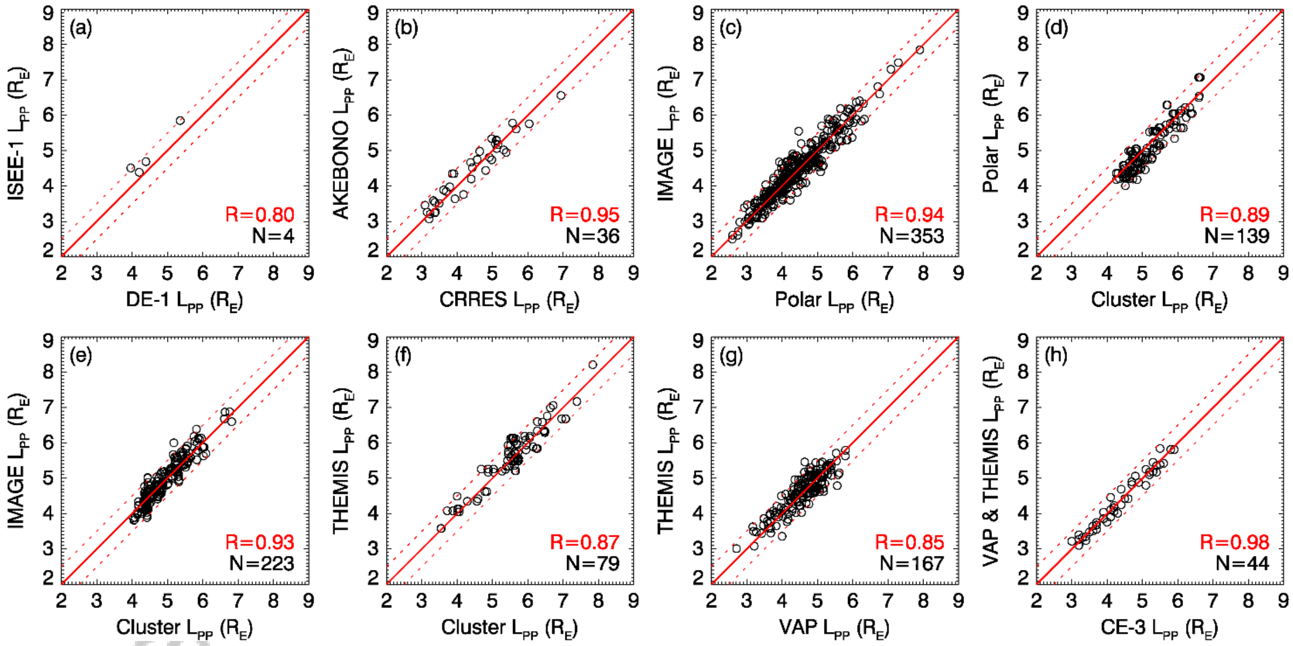

Figure 6. Comparisons between plasmapause locations that are simultaneously observed by two different satellites at the same MLTs. Satellites used in the comparison in each panel are labeled as the titles of the corresponding axes, respectively. The red solid and dashed lines indicate perfect agreement and errors of ±0.5 R_E, respectively. Black and red numbers in each panel denote the number of circles and the linear correlation coefficient, respectively.

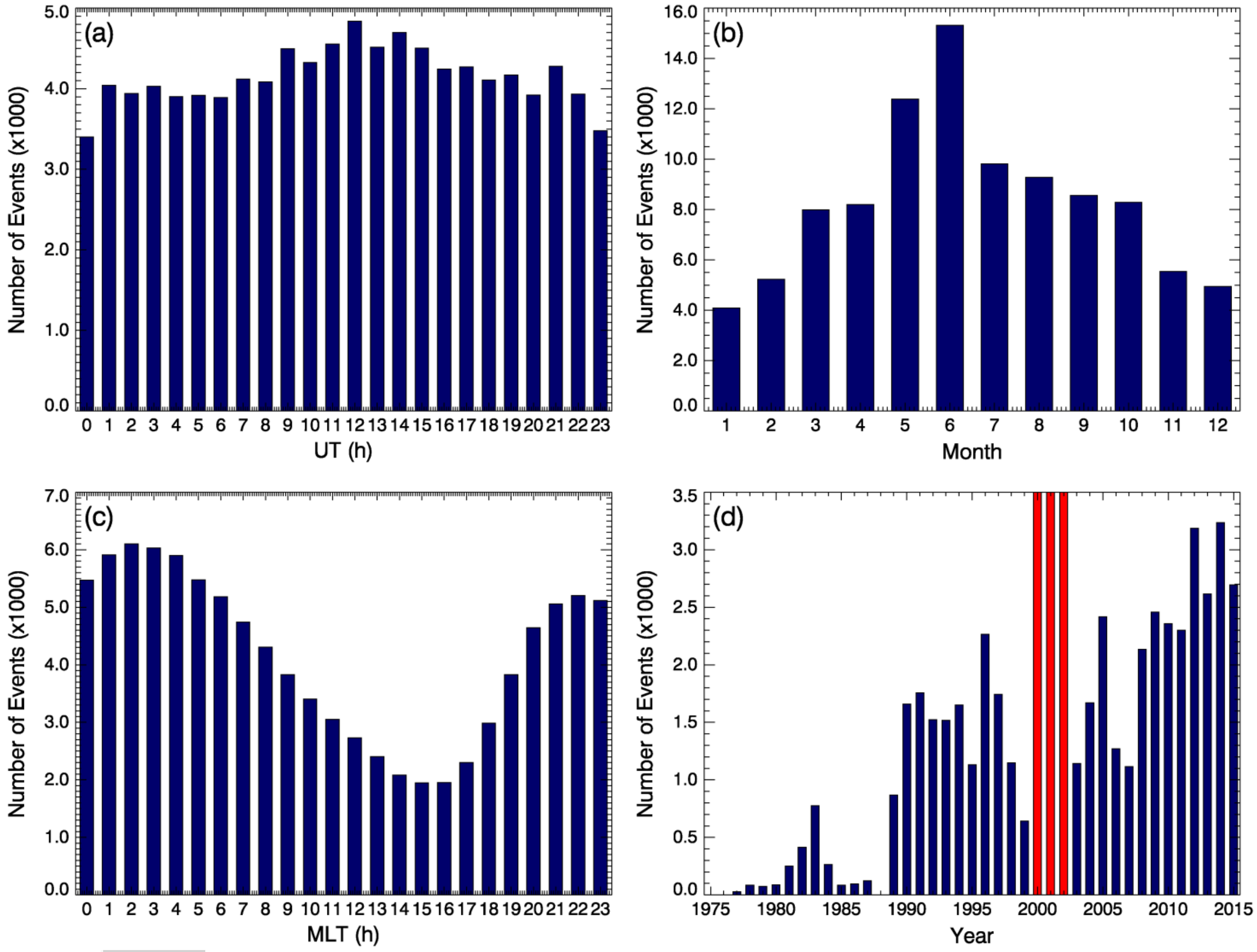

Figure 7. Distributions of the plasmapause locations versus (a) UT, (b) month, (c) MLT and (d) year. The numbers of events for the three red histograms in (d) are 16163, 24140, and 12594, respectively, due to the large number of events from IMAGE EUV.

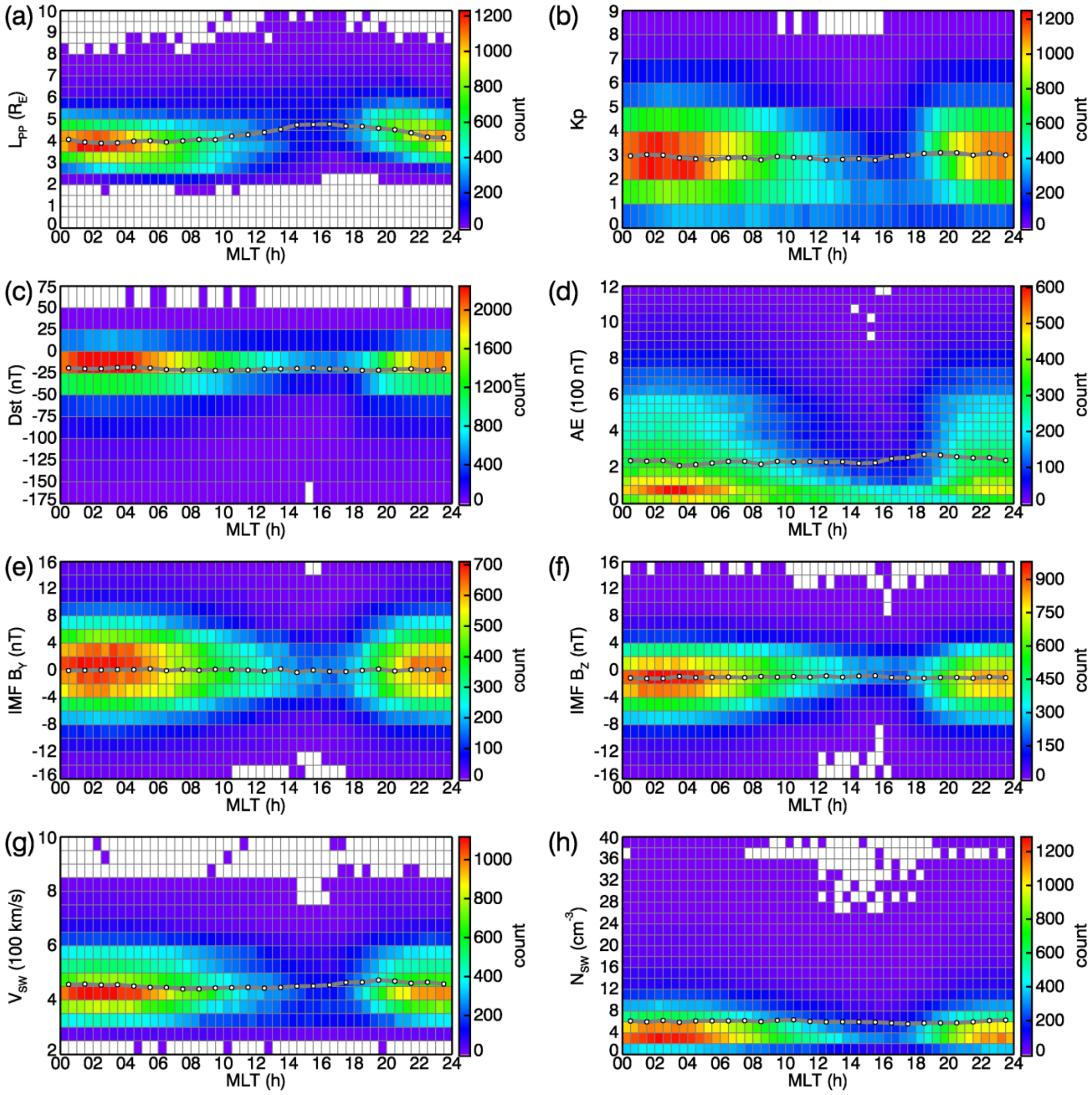

Figure 8. MLT distributions (0.5 h bins) of the plasmapause events on (a) L-value (0.5 R_E bins), (b) Kp index (1.0 bins), (c) Dst index (25 nT bins), (d) AE index (50 nT bins), (e) IMF B_Y, y component of IMF in GSM coordinate system (2 nT bins), (f) IMF B_Z, z component of IMF in GSM coordinate system (2 nT bins), (g) V_{SW}, solar wind flow speed (50 km/s bins), and (h) N_{SW}, solar wind density (2.0 cm^{-3} bins). The thick dotted lines in each panel represent average values in 1 h bins. Note that each panel has a different color bar, which is scaled as shown to the right of each panel.

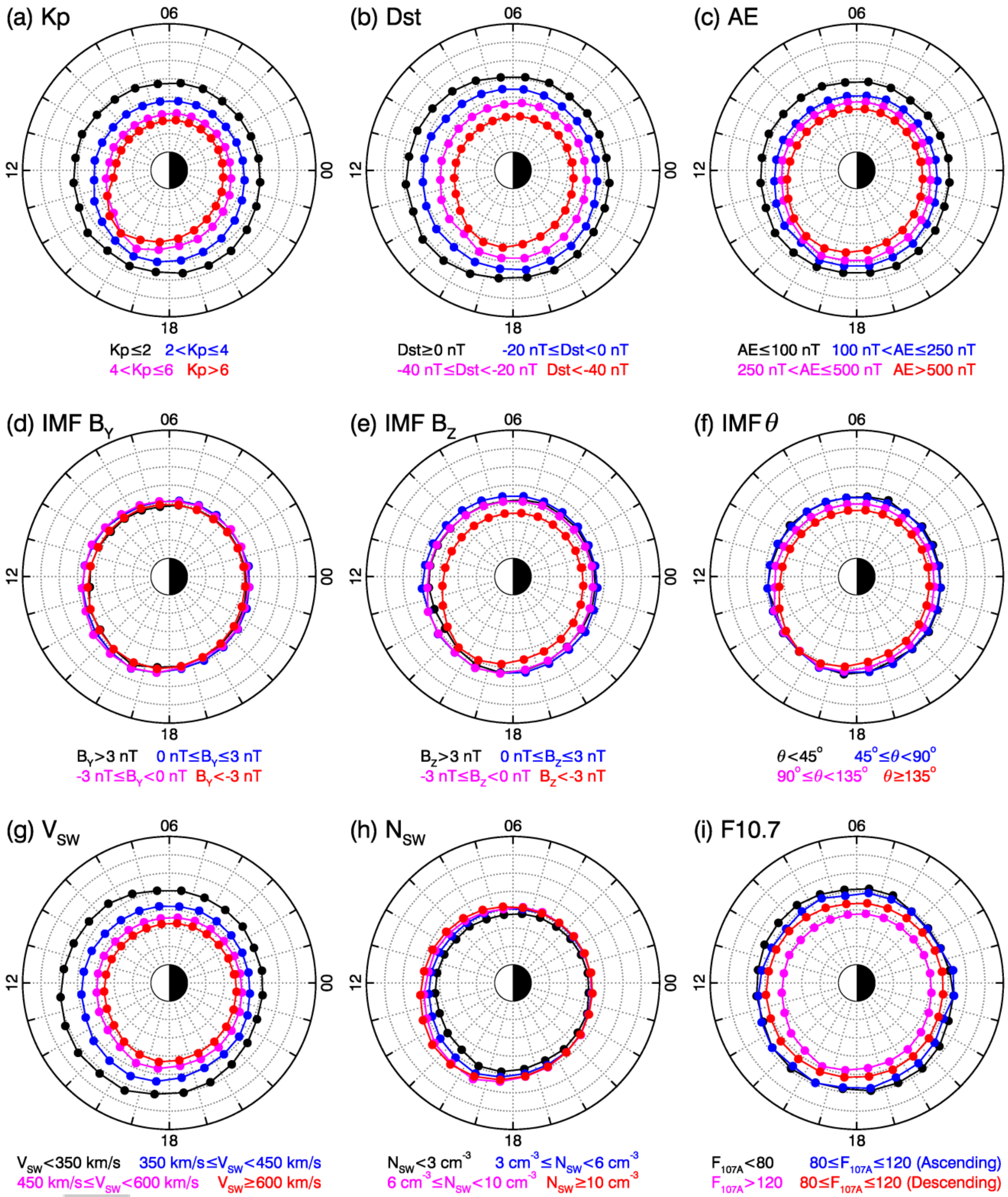

Figure 9. Global shapes of the plasmapause for different levels of activity, parameterized by (a) *Kp*, (b) *Dst*, (c) *AE*, (d) IMF B_Y, (e) IMF B_Z, (f) IMF clock angle θ, (g) V_{SW}, (h) N_{SW}, and (i) F107,

respectively. The dotted circles are drawn from 2.0 R_E to 7.0 R_E with 1 R_E intervals. The dotted radial lines are drawn in 1 h MLT intervals. Different colors representing different levels of activity are shown at the bottom of each panel.

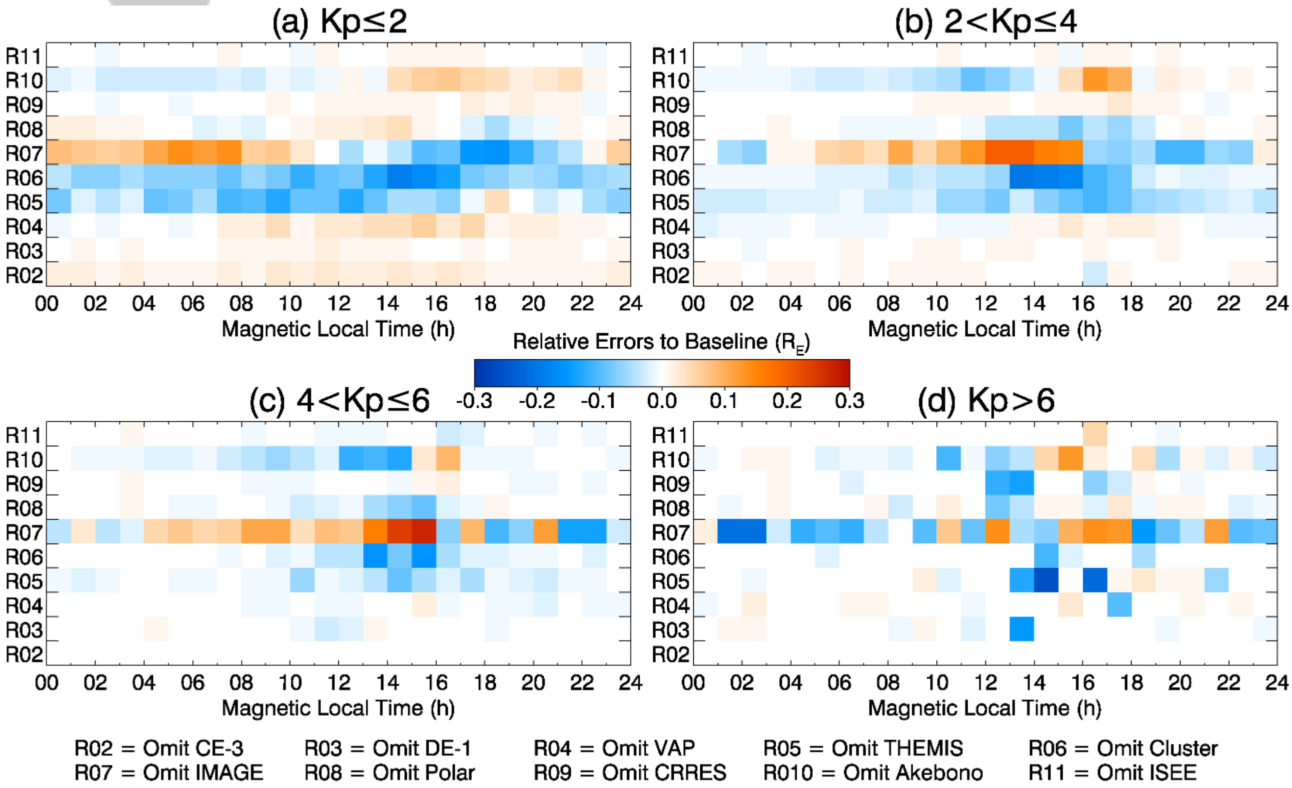

Figure 10. Relative errors of R02 – R11 to R01 (baseline).

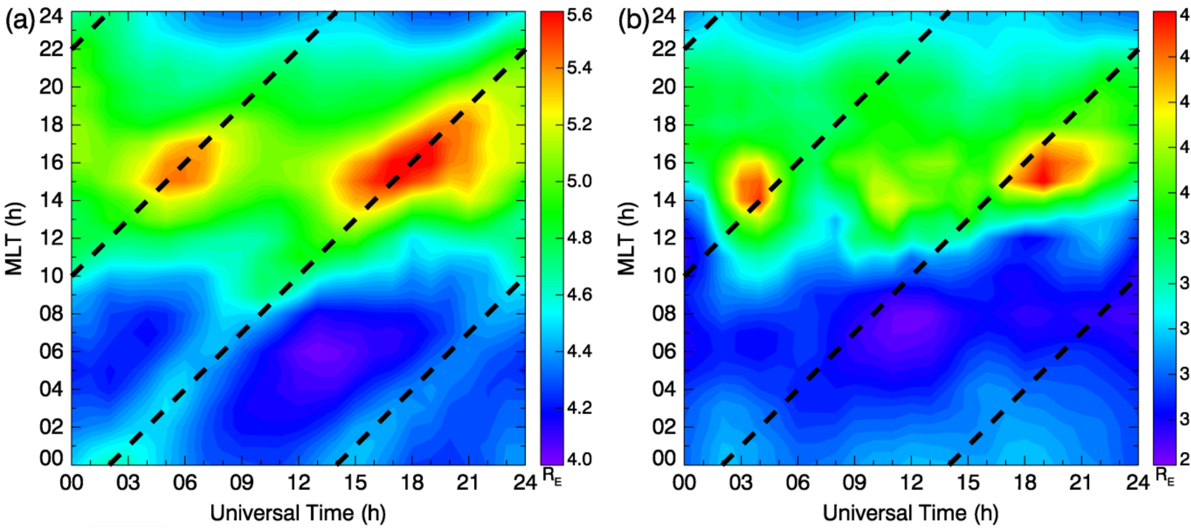

Figure 11. The contour plot of the diurnal MLT variations of the plasmapause for (a) $Kp < 4$ and (b) $Kp \geq 4$, in R_E with the color bar shown at the right, respectively. The dashed lines are drawn at slopes of dMLT / dUT = 1.0, indicating the same shift rate in both MLT and UT (i.e., perfect corotation).

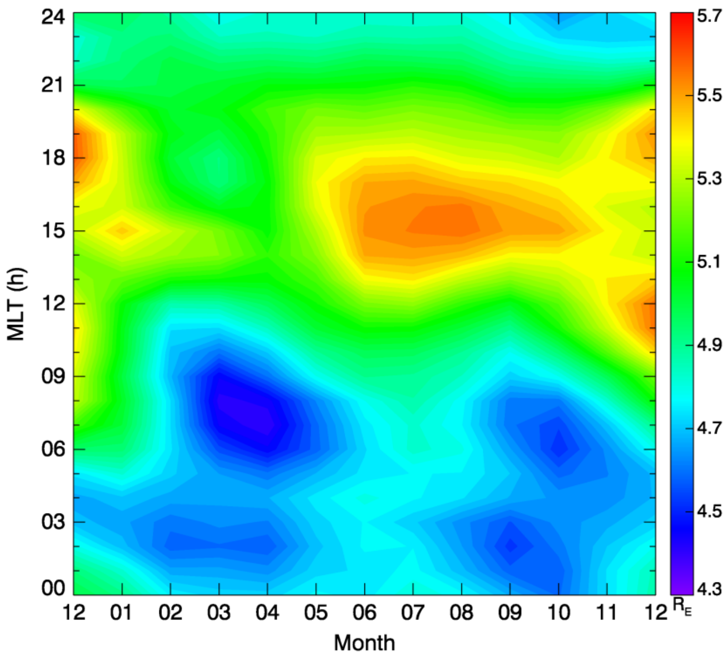

Figure 12. The contour plot of the seasonal MLT variations of the plasmapause in R_E with the color bar shown at the right.

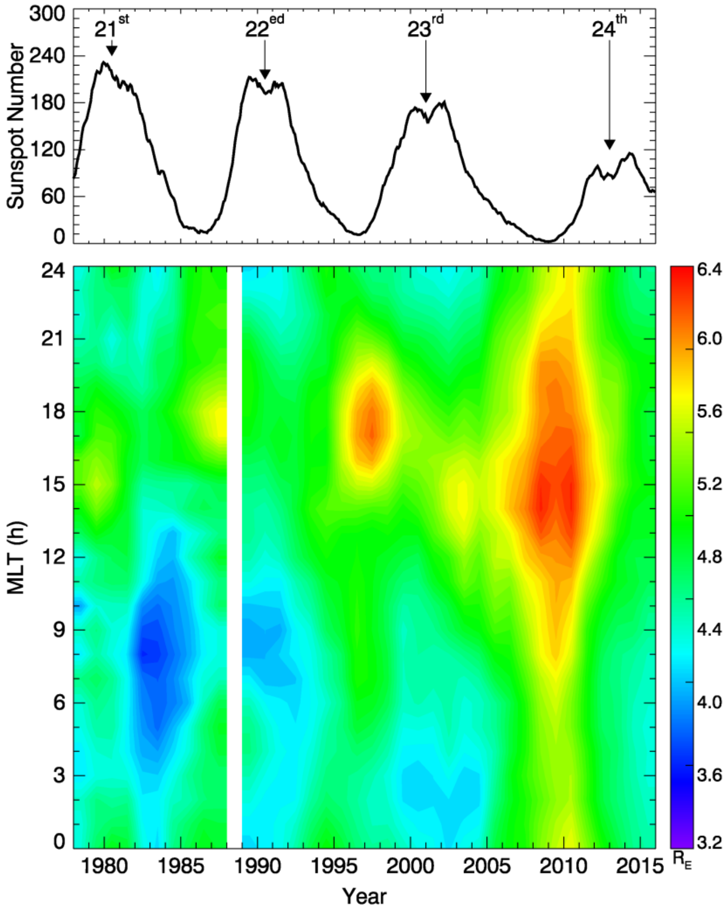

Figure 13. (*top*) Plot of the monthly averaged sunspot numbers for solar cycles 21-24 as marked by the vertical arrows. (*bottom*) The contour plot of the yearly MLT variations of the plasmapause, in R_E, with the color bar is shown at the right.

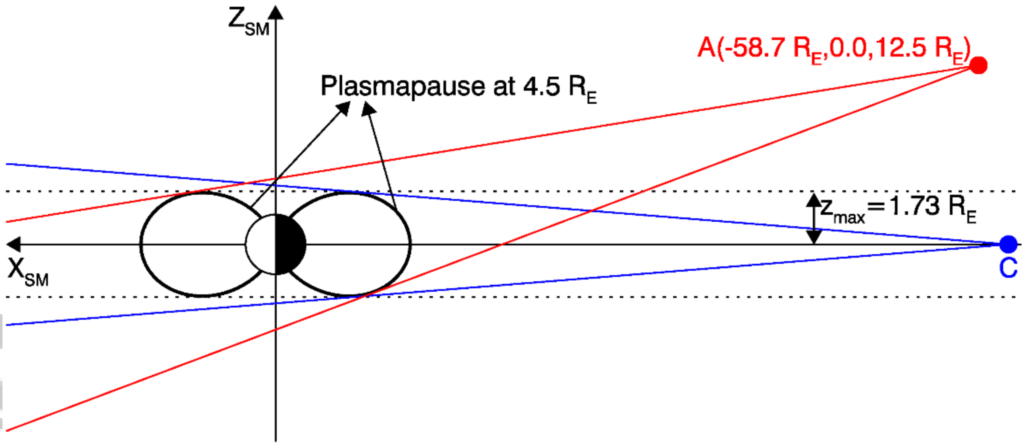

Figure A1. Illustration of the LOS configurations for different imaging positions in noon-midnight meridian plane in the SM coordinate system.

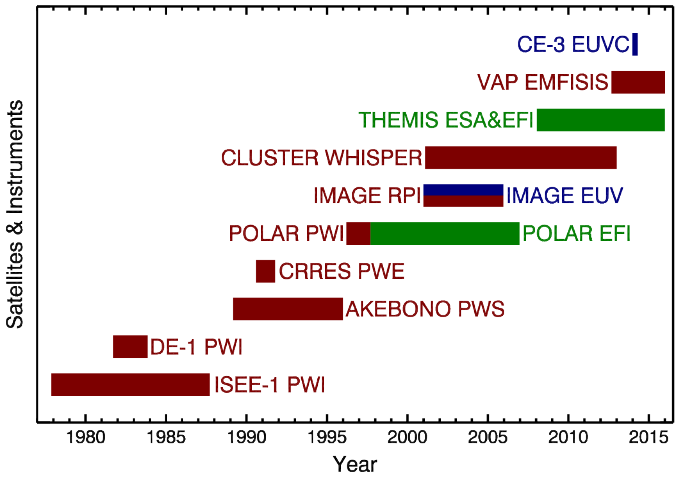

2017ja023912-f01-z-.eps

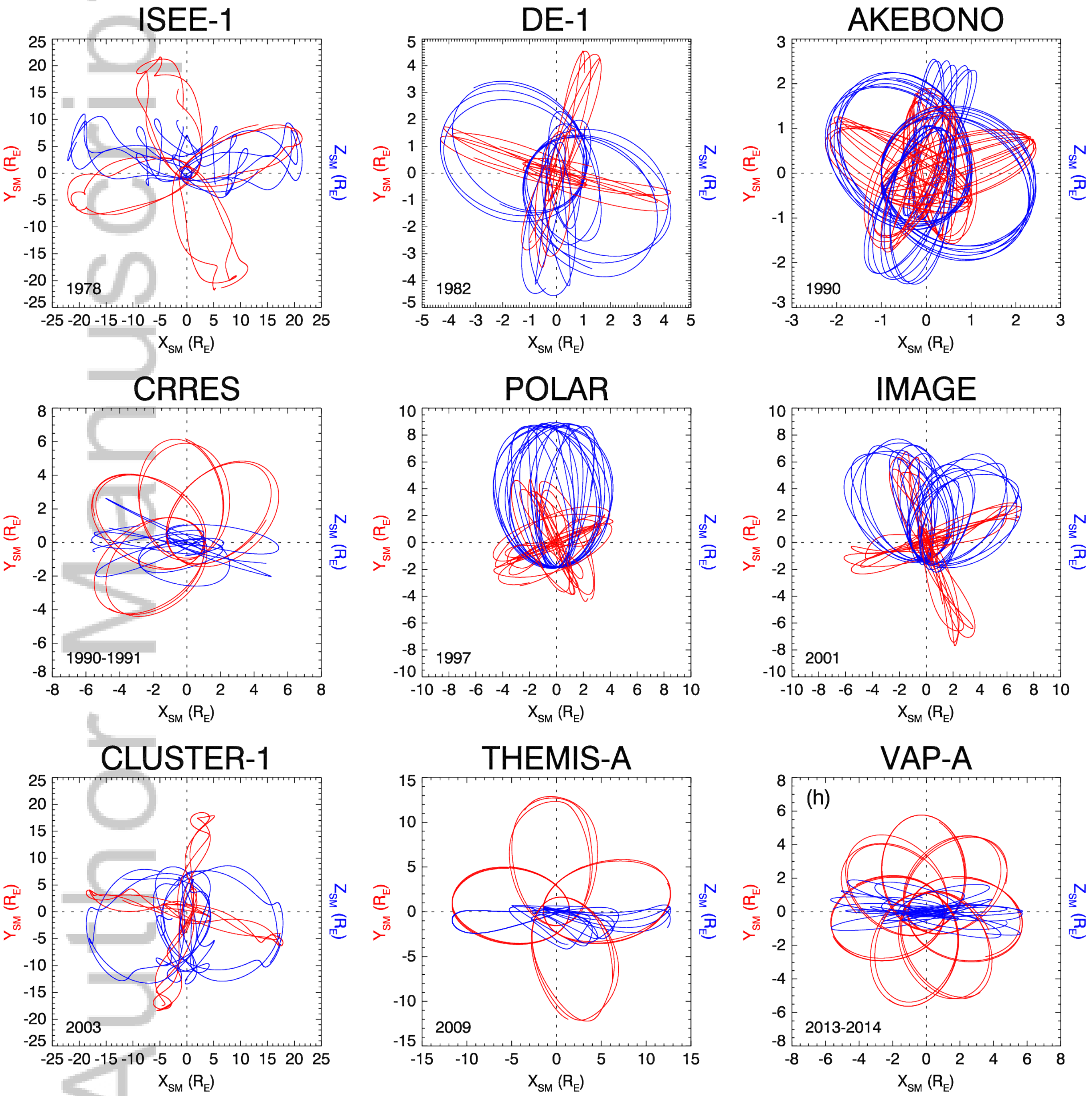

2017ja023912-f02-z-.eps

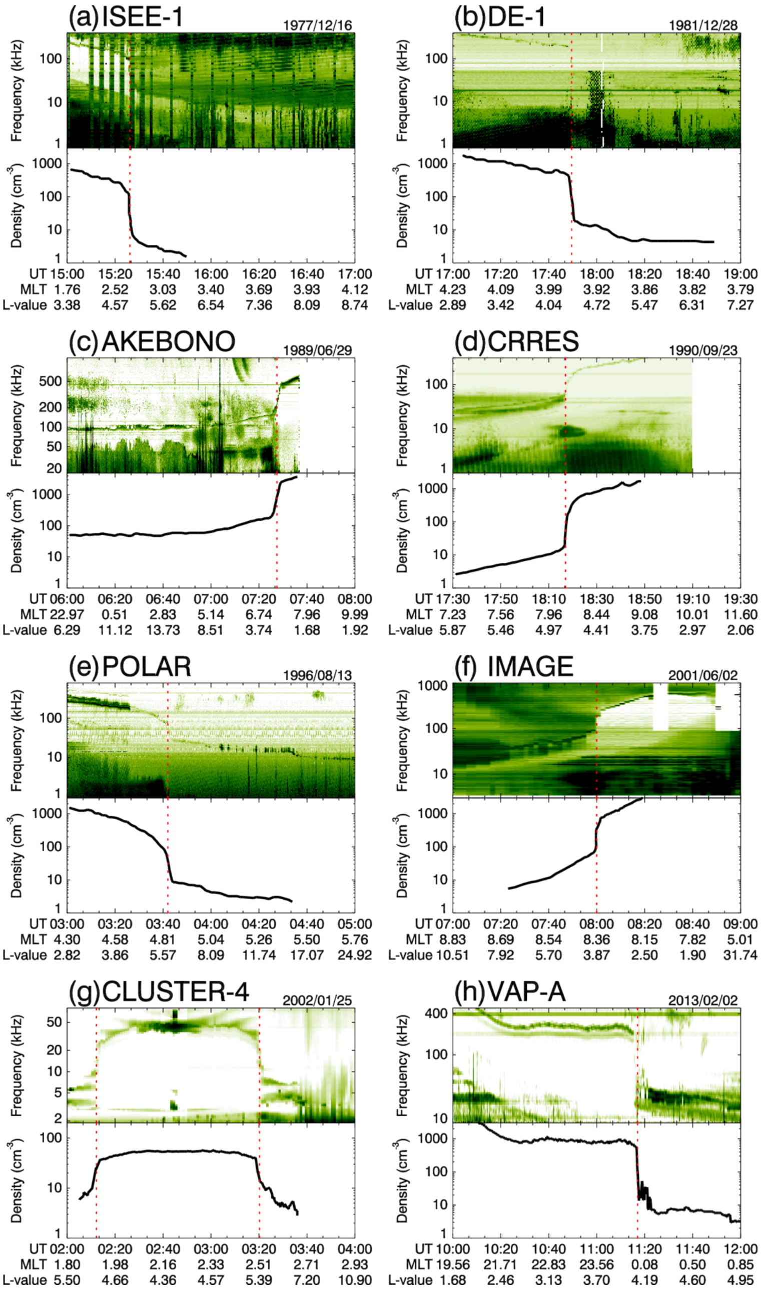

2017ja023912-f03-z-.eps

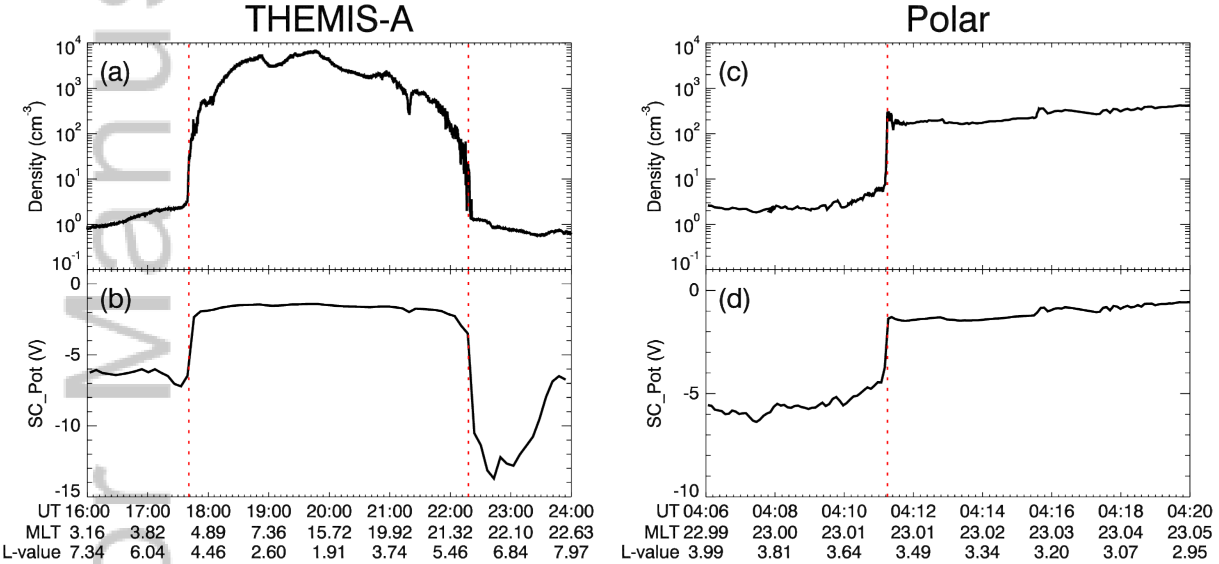

2017ja023912-f04-z-.eps

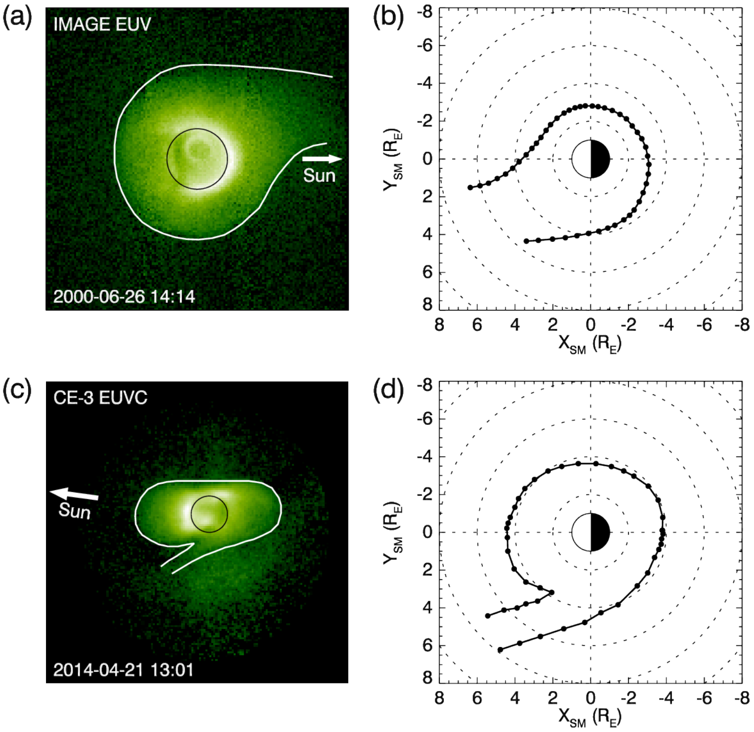

2017ja023912-f05-z-.eps

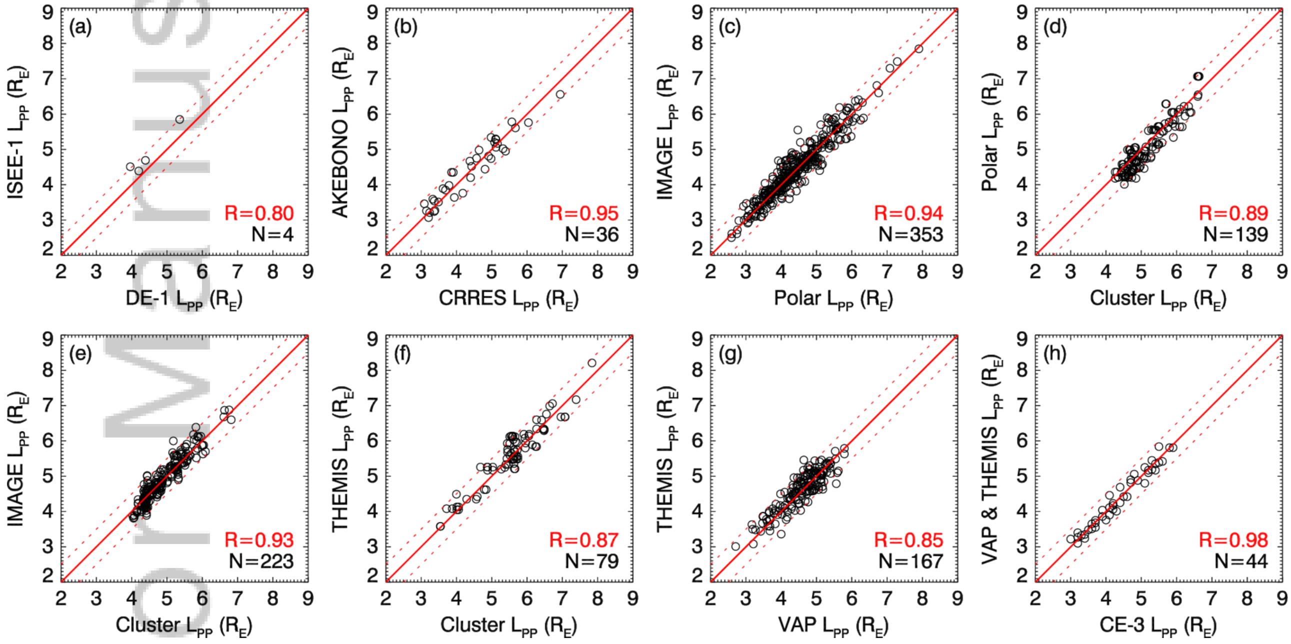

2017ja023912-f06-z-.eps

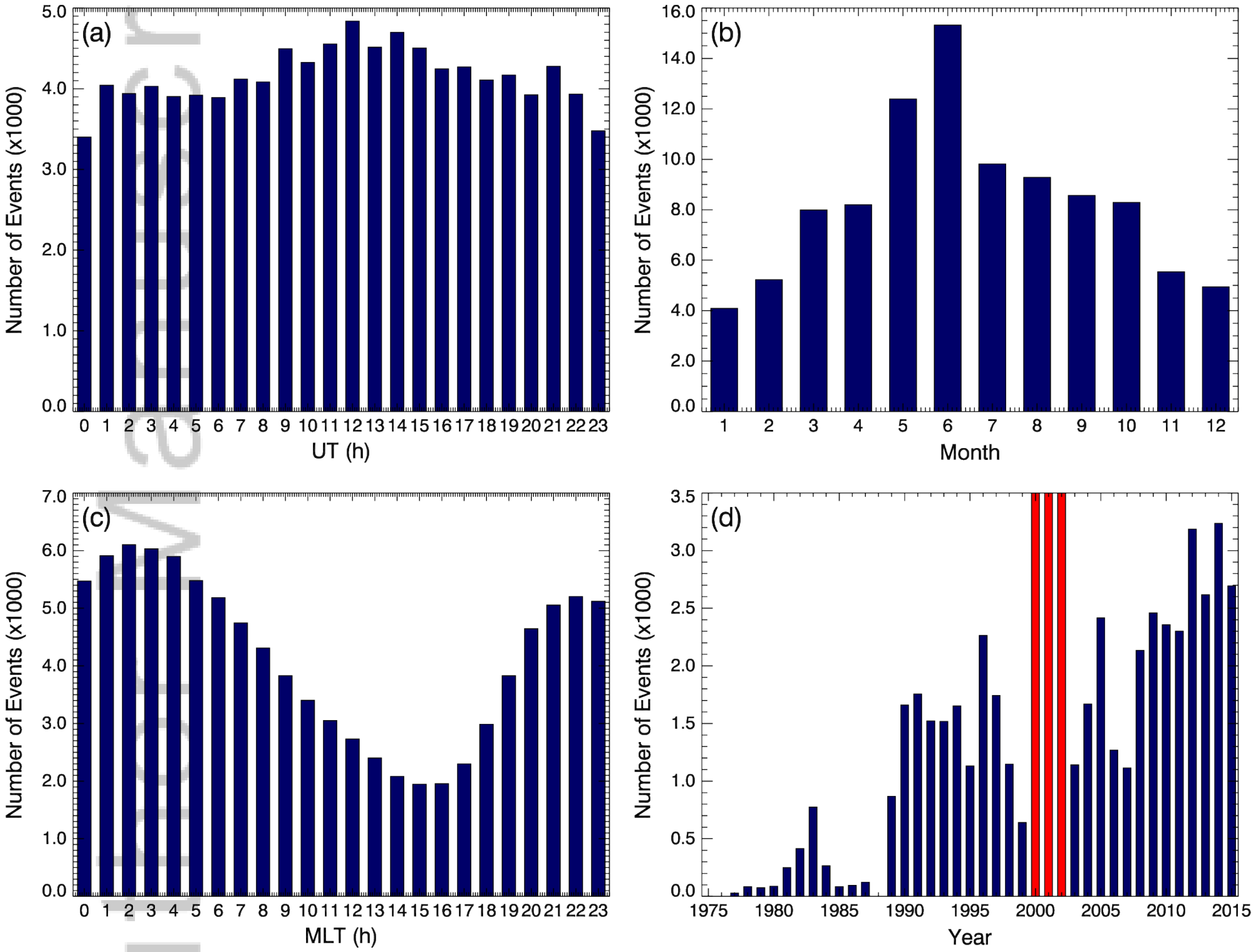

2017ja023912-f07-z-.eps

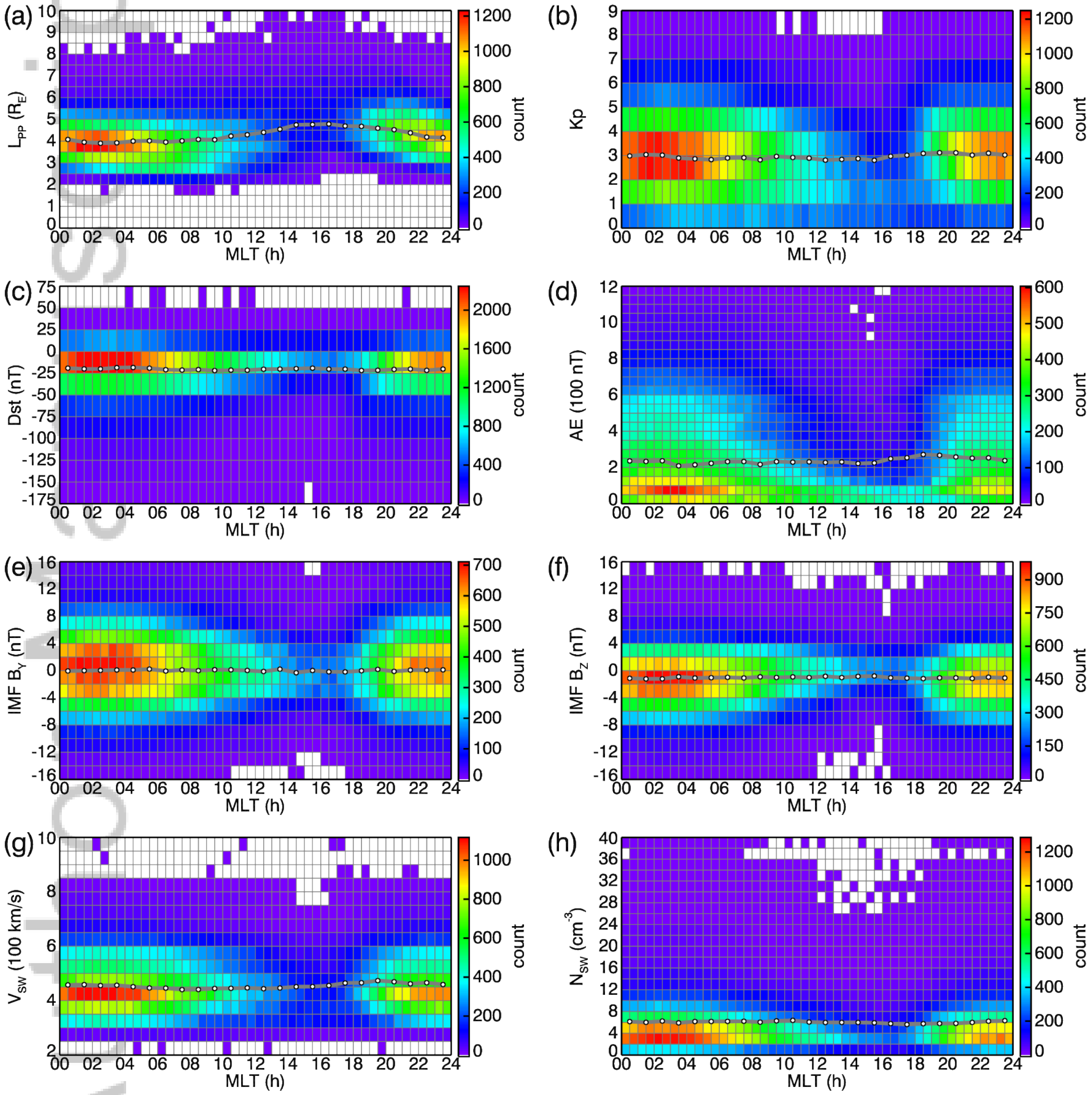

2017ja023912-f08-z-.eps

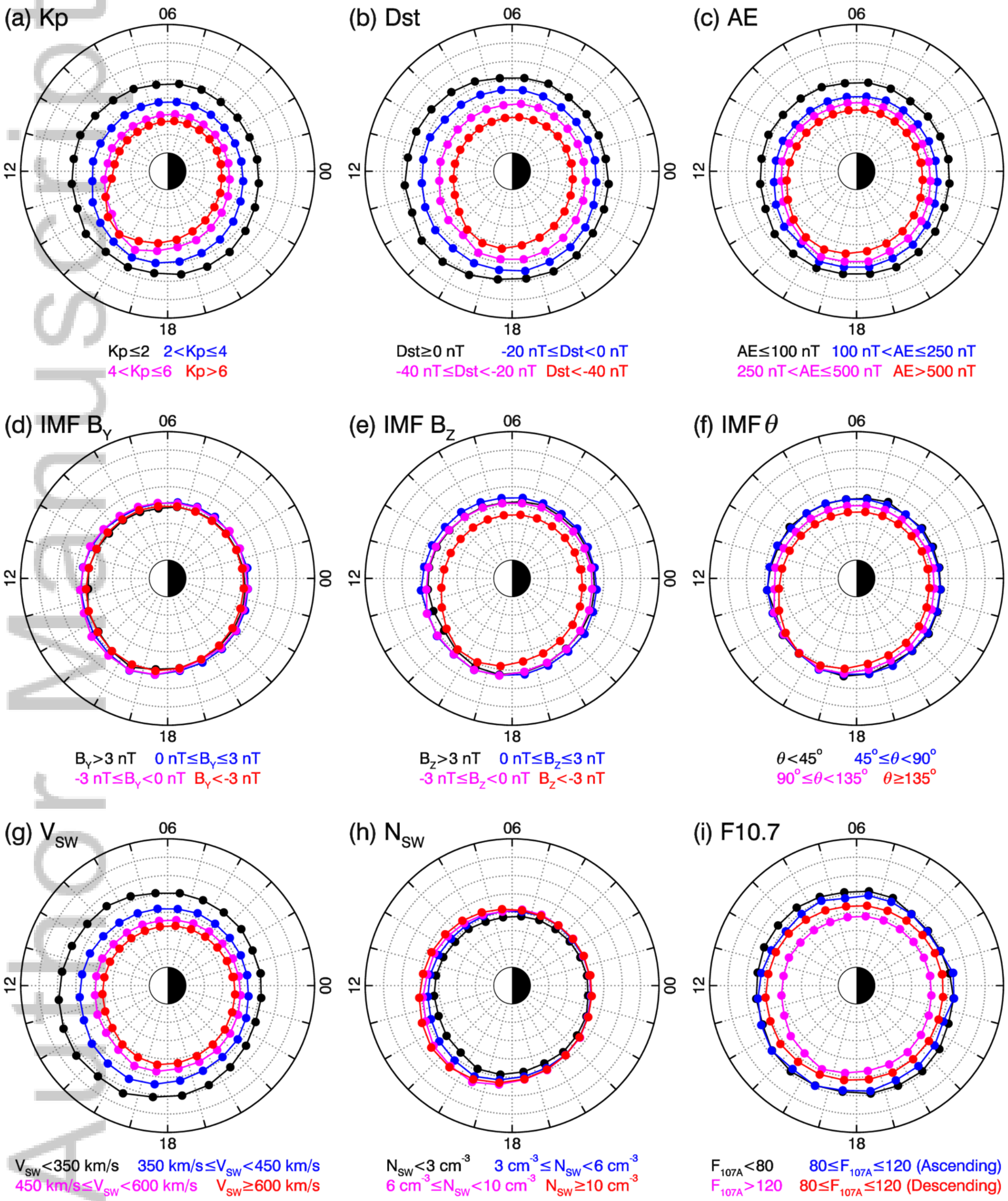

2017ja023912-f09-z-.eps

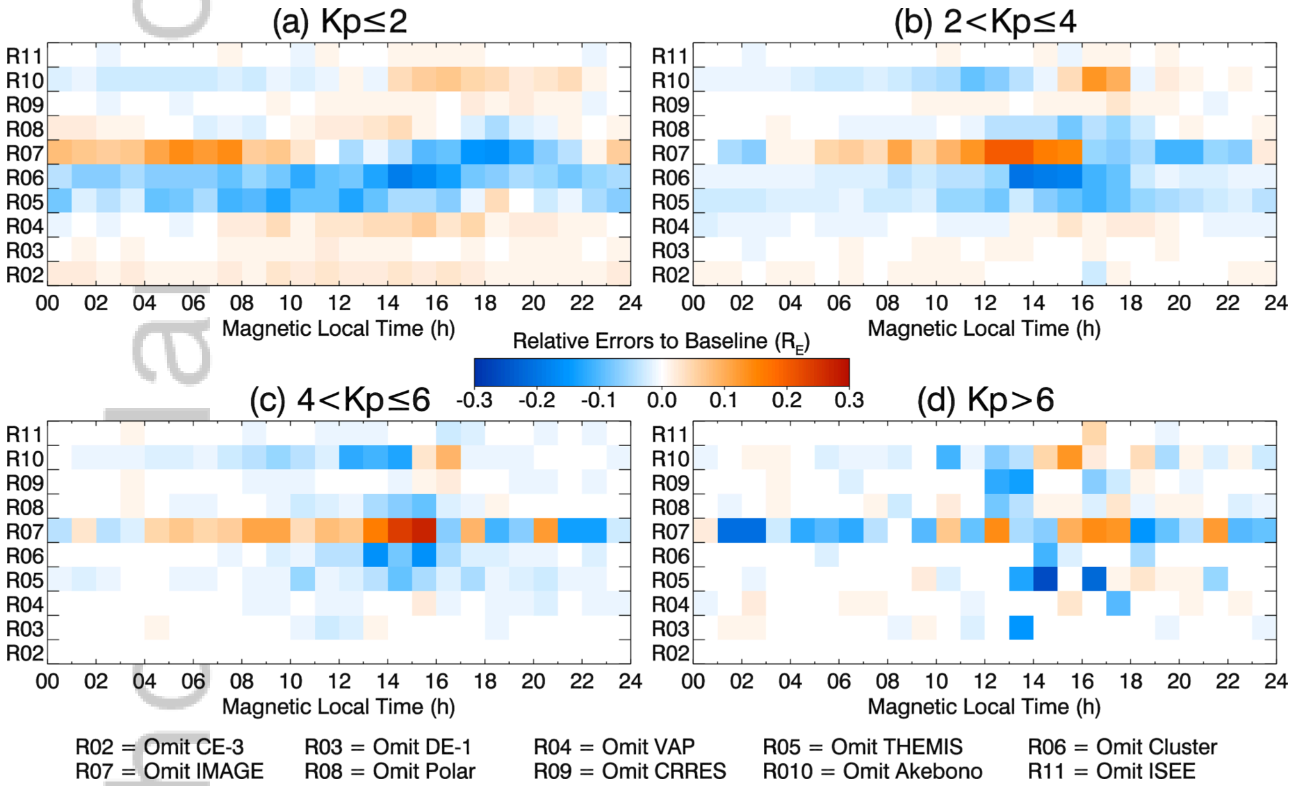

2017ja023912-f10-z-.eps

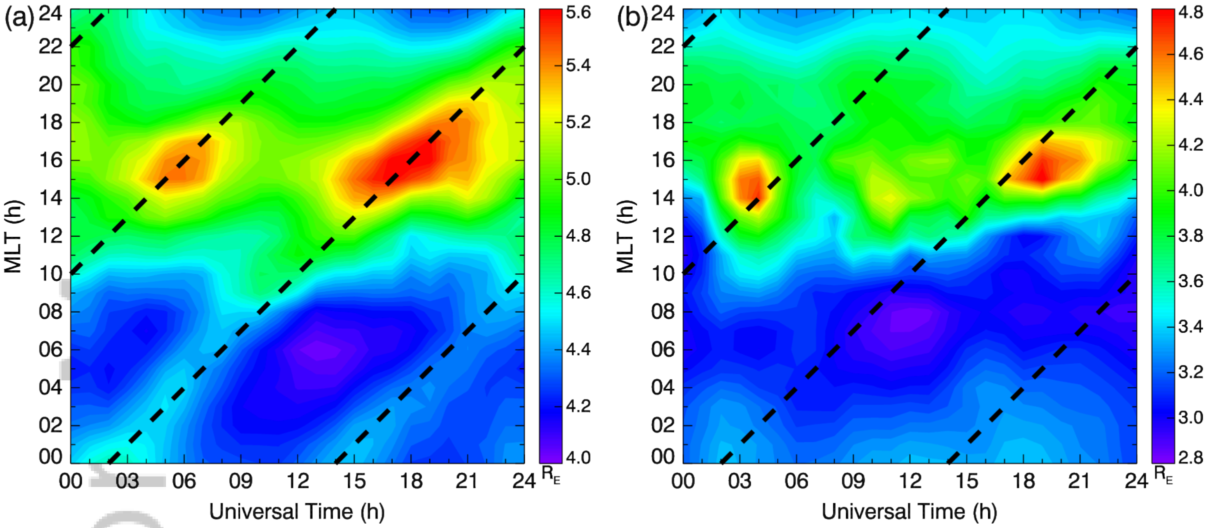

2017ja023912-f11-z-.eps

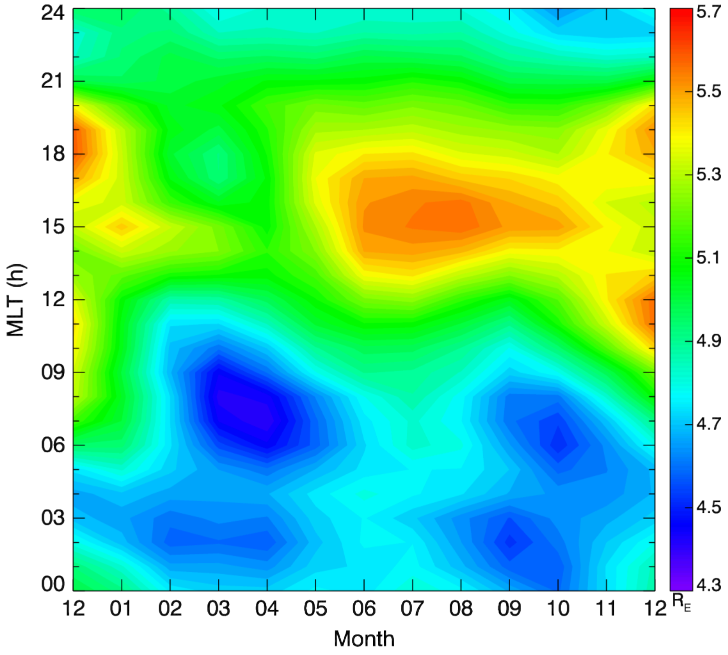

2017ja023912-f12-z-.eps

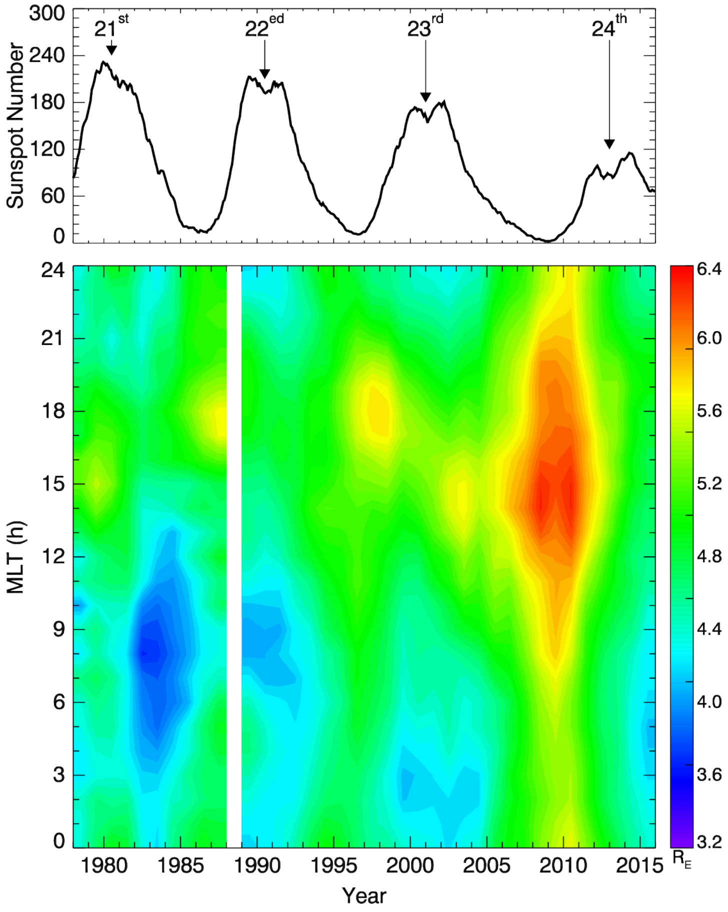

2017ja023912-f13-z-.eps

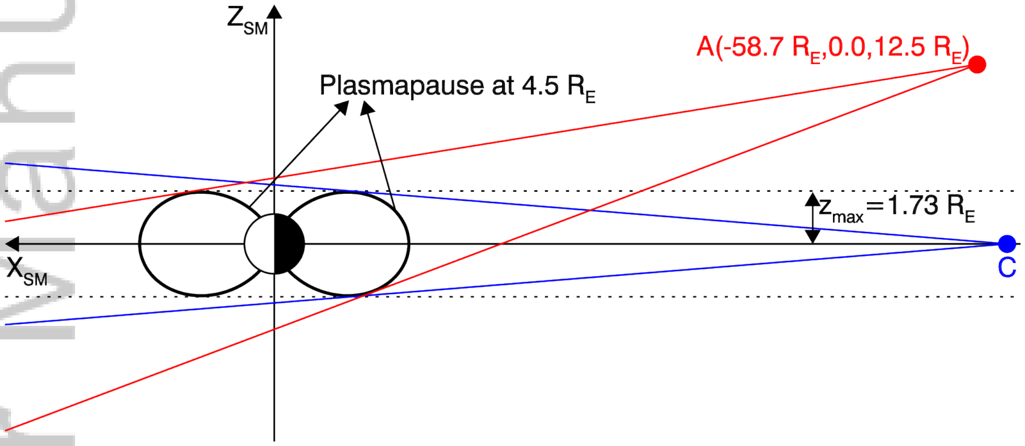

2017ja023912-f14-z-.eps